## RESEARCH ARTICLE

**Key Points:**
- MIPAS $CO_2$ concentrations in the upper atmosphere are validated against ACE-FTS and SABER measurements
- MIPAS agrees very well with ACE and SABER below 100 km; at 100–120 km ACE is larger than MIPAS (20–40%), while MIPAS and SABER are within 20%
- MIPAS and SD-WACCM $CO_2$ are in very good agreement below 100 km, but WACCM is generally larger in about 20–60% at 100-130 km.

**Supporting Information:**
- Supporting Information S1

**Correspondence to:**
M. López-Puertas,
puertas@iaa.es

# Validation of the MIPAS $CO_2$ volume mixing ratio in the mesosphere and lower thermosphere and comparison with WACCM simulations

Manuel López-Puertas[1] [ID], B. Funke[1] [ID], Á. A. Jurado-Navarro[1] [ID], M. García-Comas[1] [ID], A. Gardini[1], C. D. Boone[2], L. Rezac[3,4] [ID], and R. R. Garcia[5] [ID]

[1]Instituto de Astrofísica de Andalucía, CSIC, Granada, Spain, [2]Department of Chemistry, University of Waterloo, Waterloo, Ontario, Canada, [3]Max-Planck-Institut für Sonnensystemforschung, Göttingen, Germany, [4]Center for Atmospheric Science, Hampton University, Hampton, Virginia, USA, [5]National Center for Atmospheric Research, Boulder, Colorado, USA

**Abstract** We present the validation of Michelson Interferometer for Passive Atmospheric Sounding (MIPAS) $CO_2$ daytime concentration in the mesosphere and lower thermosphere by comparing with Atmospheric Chemistry Experiment (ACE) Fourier transform spectrometer and Sounding of the Atmosphere using Broadband Emission Radiometry (SABER) data. MIPAS shows a very good agreement with ACE below 100 km with differences of ∼5%. Above 100 km, MIPAS $CO_2$ is generally lower than ACE with differences growing from ∼5% at 100 km to 20–40% near 110–120 km. Part of this disagreement can be explained by the lack of a nonlocal thermodynamic equilibrium correction in ACE. MIPAS also agrees very well (∼5%) with SABER below 100 km. At 90–105 km, MIPAS is generally smaller than SABER by 10–30% in the polar summers. At 100–120 km, MIPAS and SABER $CO_2$ agree within ∼10% during equinox but, for solstice, MIPAS is larger by 10–25%, except near the polar summer. Whole Atmosphere Community Climate Model (WACCM) $CO_2$ shows the major MIPAS features. At 75–100 km, the agreement is very good (∼5%), with maximum differences of ∼10%. At 95–115 km MIPAS $CO_2$ is larger than WACCM by 20–30% in the winter hemisphere but smaller (20–40%) in the summer. Above 95–100 km WACCM generally overestimates MIPAS $CO_2$ by about 20–80% except in the polar summer where underestimates it by 20–40%. MIPAS $CO_2$ favors a large eddy diffusion below 100 km and suggests that the meridional circulation of the lower thermosphere is stronger than in WACCM. The three instruments and WACCM show a clear increase of $CO_2$ with time, more markedly at 90–100 km.

## 1. Introduction

Carbon dioxide is an important greenhouse gas playing an essential role in the energy budget of the atmosphere. In particular, it is responsible for the large radiative cooling of the upper mesosphere and lower thermosphere, and hence, it is one of the major drivers of the temperature of these atmospheric regions [*López-Puertas and Taylor*, 2001; *Garcia et al.*, 2014]. It has been reported recently that anthropogenic $CO_2$ increases in the lower atmosphere propagate upward throughout the entire atmosphere [*Emmert et al.*, 2012; *Yue et al.*, 2015; *Garcia et al.*, 2016]. This should result in a cooler, more contracted thermosphere [*Roble and Dickinson*, 1989; *Laštovička et al.*, 2011], which might reduce atmospheric drag and increase the lifetime of orbiting space debris [*Lewis et al.*, 2011; *Liou and Johnson*, 2008].

$CO_2$ in the middle and upper atmosphere, where its mixing ratio starts to decrease with height, has been measured by different techniques (see *López-Puertas et al.* [2000] for a review of the measurements carried out until 2000). It was first measured in the upper atmosphere by in situ measurements carried out by rocket-borne mass spectrometers [*Offermann and Grossmann*, 1973; *Trinks et al.*, 1978; *Trinks and Fricke*, 1978]. It was also measured by using the solar occultation technique, e.g., as taken by Atmospheric Trace Molecule Spectroscopy (ATMOS) aboard Spacelab 3 [*Rinsland et al.*, 1992], as well as by measuring the atmospheric limb emission in the near IR, mainly at 4.3 μm. The latter comprise several spaceborne instruments such as the Stratospheric and Mesospheric Sounder (SAMS) on Nimbus 7 [*López-Puertas and Taylor*, 1989], the Improved Stratospheric and Mesospheric Sounder (ISAMS) on Upper Atmosphere Research Satellite [*López-Puertas et al.*, 1998; *Zaragoza et al.*, 2000], and by the Cryogenic Infrared Spectrometers and Telescopes for the Atmosphere measurements in the 60–130 km region [*Kaufmann et al.*, 2002].

More recently, three $CO_2$ satellite data sets have been made available. The Fourier transform spectrometer on the Canadian Atmospheric Chemistry Experiment (ACE-FTS), using the solar occultation technique, has measured the $CO_2$ volume mixing ratio (vmr) in mesosphere and lower thermosphere (70 to 120 km). This technique is affected by uncertainties in the nonlocal thermodynamic equilibrium (non-LTE) parameters but only through the vibrational partition function, that is, the non-LTE population of the lowest energy $CO_2(010)$ state [*Edwards et al.*, 1998]. However, ACE has an uneven and sparse latitudinal coverage and needs a couple of months to obtain a near global latitudinal coverage [*Beagley et al.*, 2010]. Almost at the same time as ACE, the Sounding of the Atmosphere using Broadband Emission Radiometry (SABER), on board the NASA Thermosphere Ionosphere Energetics and Dynamics (TIMED), has been measuring the atmospheric limb radiance in the 15 μm and 4.3 μm broadband channels. Simultaneous retrievals of pressure-temperature and $CO_2$ vmr in the middle and upper atmosphere have been retrieved from these measurements [*Rezac et al.*, 2015a, 2015b].

The third set of satellite measurements has been made available recently from the inversion of Michelson Interferometer for Passive Atmospheric Sounding (MIPAS) high-resolution limb emission spectra in the 4.3 $\mu$m region [*Jurado-Navarro et al.*, 2016]. MIPAS is able to discriminate the contributions of the many $CO_2$ bands that give rise to the 4.3 μm atmospheric emission and thus has allowed us to improve our knowledge of the $CO_2$ non-LTE processes that control the population of the emitting levels near 4.3 μm [*Jurado-Navarro et al.*, 2015]. This, in turn, permits to retrieve $CO_2$ from limb emission observations with better accuracy. Furthermore, the wide spectral range of MIPAS enabled us to retrieve the temperature up to about 100 km from the $CO_2$ 15 μm region [*García-Comas et al.*, 2012, 2014] and also in the lower thermosphere (up to about 170 km) from the spectrally resolved NO 5.3 μm emissions [*Bermejo-Pantaleón et al.*, 2011]. The availability of these temperature measurements, required for an accurate non-LTE and radiative transfer modeling, has allowed us to retrieve global distributions of the $CO_2$ vmr in the mesosphere and lower thermosphere (from 75 km up to ~140 km).

$CO_2$ vmr from ACE and SABER measurements has already been compared to each other [*Rezac et al.*, 2015b]. Our goal here is to compare MIPAS with ACE and SABER measurements in order to validate the former and to detect possible systematic biases among the three instruments, all using different techniques. ACE is a solar occultation instrument, while SABER and MIPAS are measuring in emission. Thus, while ACE is affected by non-LTE only through the $CO_2(010)$ state (see above), MIPAS and SABER are affected mainly through the non-LTE populations of the states emitting near 4.3 μm. Also, while SABER and MIPAS both measure in emission, the former is a wideband radiance instrument, but the latter is a high-resolution spectrometer which, in principle, should provide more information.

Additionally, we compare the $CO_2$ observations of MIPAS with simulations made using the Whole Atmosphere Community Climate Model (WACCM) in the upper atmosphere. Above about 120 km the $CO_2$ vmr has not been measured globally before, and hence, we expect to improve our understanding of the dynamics and chemistry of these atmospheric layers.

The paper is arranged as follows. In sections 2–4 we describe the $CO_2$ measurements of MIPAS, ACE, and SABER, respectively, and in section 5 the WACCM model simulations. Section 6 describes the comparison between the three instruments and section 7 the comparison of MIPAS observations with WACCM-SD simulations. The major conclusions are summarized in section 9.

## 2. MIPAS Data

The MIPAS instrument is a mid-infrared limb emission spectrometer designed and operated for measurements of atmospheric trace species from space [*Fischer et al.*, 2008]. It was part of the payload of Envisat launched on 1 March 2002 with a Sun-synchronous polar orbit of 98.55°N inclination and an altitude of 800 km. MIPAS had a global coverage from pole to pole passing the equator from north to south at 10:00 A.M. local time 14.3 times a day and taking daytime and nighttime profiles of spectra. The instrument's field of view is 30 km in horizontal and approximately 3 km in vertical direction. From January 2005 to the end of Envisat's operations on 8 April 2012, MIPAS measured at an optimized spectral resolution of 0.0625 cm$^{-1}$. MIPAS sounded the middle and upper atmospheres in three measurements modes: MA (middle atmosphere), NLC (noctilucent clouds), and UA (upper atmosphere). The latter was specifically devised for measuring the thermospheric temperature and composition (CO, $CO_2$, and NO) and scanned the limb from 42 to 172 km.

Here we use the global distributions of the $CO_2$ vmr in the mesosphere and lower thermosphere (from 75 km up to 140 km) (version v5r_$CO_2$_622) that have been retrieved from the daytime MIPAS spectra in the 4.3 μm

region taken in the UA observation mode [*Jurado-Navarro et al.*, 2016]. The data set spans from January 2005 to March 2012. A few observations were taken during 2005, 2006, and in the first half of 2007 and then continuously from May 2007 to March 2012 with a cadence of about 1 out of 10 days. For the analysis carried out in this work we excluded profile data with little to no sensitivity characterized by values of the diagonal element of the averaging kernel smaller than 0.03. A few profiles were additional removed that presented large residuals ($\chi^2 > 2.3$). Daytime data were considered rather strict, with solar zenith angle smaller than 80° in order to avoid errors due to inhomogeneous illumination along the line of sight.

The retrieval of $CO_2$ has been performed jointly with the elevation pointing of the line of sight (LOS) by using a non-LTE retrieval scheme. The retrieval strategy is a constrained multiparameter nonlinear least squares fitting of measured and modeled spectra, which is described in detail by *von Clarmann et al.* [2003]. Its extension to retrievals under consideration of non-LTE is described in *Funke et al.* [2001]. The non-LTE vibrational populations of $CO_2$ are modeled with the Generic RAdiative traNsfer AnD non-LTE population Algorithm [*Funke et al.*, 2012] within each iteration of the retrieval but incorporating the new collisional rates recently derived from the MIPAS spectra by *Jurado-Navarro et al.* [2015]. A more detailed description of the MIPAS $CO_2$ retrieval can be found in *Jurado-Navarro et al.* [2016].

The MIPAS $CO_2$ retrieval also takes advantage of simultaneous MIPAS measurements of other atmospheric parameters, as the kinetic temperature, derived from the stratosphere up to ~100 km from the 15 μm spectral region [*García-Comas et al.*, 2014] and from 100 km up to 170 km from the NO 5.3 μm emission [*Bermejo-Pantaleón et al.*, 2011], and the $O_3$ measurements (up to ~100 km) [*Gil-López et al.*, 2005; *Smith et al.*, 2013]. The latter is very important for the calculations of the non-LTE populations of $CO_2$ because it strongly constrains the $O(^3P)$ and $O(^1D)$ concentrations below ~100 km. Above this altitude, $O(^3P)$ and $O(^1D)$ concentrations were taken from the WACCM model. The inclusion of those parameters in the retrieval, together with the new rate coefficients recently derived from MIPAS, leads to a substantial improvement in the accuracy of the retrieved $CO_2$. Furthermore, the inclusion of the LOS as a joint fit parameter also improves the retrieval of $CO_2$ and reduces significantly the systematic errors [*Jurado-Navarro et al.*, 2016].

The estimated precision of the retrieved $CO_2$ vmr profiles varies with altitude ranging from ~1% below 90 km to 5% around 120 km and larger than 10% above 130 km [*Jurado-Navarro et al.*, 2016]. There are some latitudinal and seasonal variations of the precision, which are mainly driven by the solar illumination conditions. The retrieved $CO_2$ profiles have a vertical resolution of about 5–7 km below 120 km and between 10 and 20 km at 120–140 km.

The major systematic error is the uncertainty of the pressure/temperature profiles, inducing errors at midlatitude conditions of up to 15% above 100 km (20% for polar summer) and of ~5% around 80 km. The errors due to uncertainties in the $O(^1D)$ and $O(^3P)$ profiles are within 3–4% in the 100–120 km region, and those due to uncertainties in the gain calibration and in the near-IR solar flux are within ~2% at all altitudes [*Jurado-Navarro et al.*, 2016].

## 3. ACE Data

The ACE-FTS has performed infrared solar occultation measurements from the SciSat satellite since 21 February 2004 following its launch on 12 August 2003 [*Bernath et al.*, 2005]. The instrument is a Fourier transform spectrometer operating between 750 and 4400 cm$^{-1}$ with a spectral resolution of 0.02 cm$^{-1}$. The SciSat satellite is in a highly inclined circular orbit (74°) and thus provides measurements from 85°N to 85°S over each year with a significant focus on polar measurements. Up to 30 measurements are made each day by ACE-FTS extending from the cloud tops to ~150 km. From these sets of spectra, profiles of over 30 trace gases and isotopologues, temperature, and pressure are retrieved. For this study, version 3.6 of the ACE-FTS data set was used.

The ACE-FTS retrieval algorithm is described in *Boone et al.* [2005], and the specific details of version 3.6 are provided in *Beagley et al.* [2010] and *Boone et al.* [2013]. Briefly, an unconstrained nonlinear least squares global fitting approach is used to fit the measured and forward modeled spectra. Selected $CO_2$ lines in the spectra are used to retrieve pressure and temperature as a function of altitude which are used later to retrieve vmr profiles of various trace gases. ACE-FTS $CO_2$ vmr is retrieved from around 60 to about 120 km, and it is fixed below about 60 km in the pressure/temperature retrieval. The calculation of the a priori $CO_2$ vmr profile starts from a profile fixed for March 2004 and then grows at a rate given by the equation used by the Halogen

Occultation Experiment experiment [*Boone et al.*, 2005]. The vertical field of view is ∼3 km, but the vertical resolution of the retrieved $CO_2$ averages 3–4 km, varying from 2 to 6 km with time of the year, alternating from best to worst every other month and being the best during February and April [*Boone et al.*, 2005]. Random errors are 2.5–5%, depending on latitude, and estimated systematic errors range from 2% at the low altitudes (50–70 km) to about 5% at 90 km, 9% at 100 km, and 16% at 118.5 km [*Beagley et al.*, 2010]. We note that ACE observations are processed in geometric coordinates, the same coordinate that we use in the comparison.

Only the data flagged with quality flag = 0, i.e., no known problems [see, *Sheese et al.*, 2015], were used. A careful inspection of the selected (flag = 0) data was performed, and it was found that there still remained a few physically unrealistic profiles, with large positive gradients or very large or small values. Thus, a further screening was performed removing the profiles with values larger than 430 ppmv or smaller than 20 ppmv in the 60–120 km region. However, some unrealistic profiles were still present. Hence, a second screening was applied removing the few profiles falling outside the $\pm 5\sigma$ range of the data for the whole time period used. A detailed inspection of the ACE $CO_2$ profiles showed that above around 110–115 km quite a few of the scans unrealistically increase with altitude. This might be introduced by the assumed $CO_2$ column above the uppermost retrieved altitude. Thus, in order to avoid the potential introduction of a positive bias, we have further removed the four uppermost altitudes (4 km) below the uppermost height flagged as good in the data set (typically within 115–120 km).

## 4. SABER Data

The SABER instrument on board the TIMED satellite has been measuring the limb radiance in 10 broadband infrared channels over the altitude range from ∼400 km to the Earth's surface since 2002. The kinetic temperatures and $CO_2$ vmrs in the mesosphere and lower thermosphere have been simultaneously retrieved using SABER limb radiances at 15 and 4.3 μm under non-LTE conditions [*Rezac et al.*, 2015a].

SABER's field of view is 2 km with a vertical sampling at the limb of 0.375 km. The horizontal resolution in the limb geometry is ∼300 km. The latitude coverage is 82°N–53°S or 53°N–82°S, with alternating coverage due to the spacecraft yaw cycle of about 60 days. Here we use the SABER $CO_2$ version2_0Level2C (ftp://saber.gats-inc.com/Version2_0/-Level2C/). In this version, the two-channel algorithm was applied only for SABER daytime observations for solar zenith angles smaller than 80° and the planetary geomagnetic index, *Kp*, smaller than 4. The Level2C two-channel retrieval has been performed on a 1 km grid spacing.

The joint retrieval of temperature and $CO_2$ vmr is performed from 65 km up to 120 km. We should recall that SABER temperatures in the 100–110 km are prone to have significant errors since they depend strongly on the atomic oxygen concentration, which was not derived simultaneously from SABER measurements. We should also bear in mind though that the $CO_2$ vmr retrieval above 110 km no longer relies on the retrieved kinetic temperature but, together with $O(^3P)$ and $O(^1D)$, they are taken from the WACCM model for the given geographic conditions.

The estimated random and systematic errors are listed in Table 1 of *Rezac et al.* [2015b]. The total systematic errors are 15, 15, 12, 21, and 32% for altitudes of 70, 80, 90, 100, and 110 km, respectively. Above 110 km, the error due to $O(^1D)$ uncertainties decays quickly, but the kinetic temperature and atomic oxygen, as they are taken from the WACCM model, are expected to be contributing with larger errors than at lower altitudes. Thus, based on synthetic calculations, we estimated that the error at 110 km is a safe upper limit for the error at the 110–120 km region.

The typical vertical resolution of SABER $CO_2$ vmr varies between 4 and 12 km, depending on the season and altitude. The better resolution (4–6 km) is generally achieved during the equinoxes. In the summer high latitudes (≳60°), below 90 km, the vertical resolution is very broad, with only one value for the 65–90 km range. The mean is assigned to the 77 km altitude with a line fit in between the end points (see *Rezac et al.* [2015a] for more details). SABER $CO_2$ measurements are available from January 2002 until now.

## 5. The Whole Atmosphere Community Climate Model (WACCM)

WACCM is a global climate model with interactive chemistry that spans the range of altitude between the surface and approximately 140 km. In this study, we use the "specified dynamics" version (SD-WACCM), described by *Garcia et al.* [2014]. In SD-WACCM, winds and temperature are constrained by NASA's Modern-Era

Retrospective Analysis data [*Rienecker et al.*, 2011] everywhere below approximately 1 hPa (corresponding to ~45 km), using the procedure discussed by *Kunz et al.* [2011]. While SD-WACCM is free running above 1 hPa, *Liu et al.* [2009] have shown that the dynamics of the mesosphere and lower thermosphere are strongly influenced by the behavior of the lower atmosphere. In the following, we refer to the model simply as WACCM, with the understanding that all simulations have been carried out with the specified dynamics version. This simulation followed the REFC1D protocol of the Chemistry Climate Model Initiative [*Eyring et al.*, 2013] for the specification of time-dependent greenhouse gases and ozone-depleting substances.

Vertical mixing due to gravity wave breaking is the principal upward transport mechanism in the lower thermosphere, below ~$10^{-4}$ hPa, particularly in the global mean sense. The parameterization of small-scale gravity waves used in WACCM is described in detail by *Garcia et al.* [2016]. We should note that the vertical eddy diffusion coefficient, $K_{zz}$, calculated with WACCM depends on the parameterization of the small-scale gravity waves and also on the value assumed for the Prandtl number, $Pr$, which describes the ratio of the eddy momentum flux to the eddy flux of potential temperature or chemical species [see *Garcia et al.*, 2007]. The Prandtl number currently used in WACCM (Chemistry Climate Model Initiative) simulations is 2. This was adopted after the study of *Garcia et al.* [2014] who found that WACCM $CO_2$ and CO obtained with this value compare better to ACE CO and $CO_2$ and MIPAS CO fields than for $Pr = 4$. Here we include a comparison of WACCM $CO_2$ with MIPAS measurements that extend to higher altitudes than in *Garcia et al.* [2014]. We are interested in knowing if the best agreement with $Pr = 2$ simulations of *Garcia et al.* [2014] also holds for MIPAS $CO_2$ and, additionally, in how well are we able to reproduce the MIPAS measurements in the lower thermosphere.

The native vertical coordinate of WACCM is pressure. Hence, the MIPAS/WACCM comparison was performed on pressure levels, although the differences are plotted in geometric altitudes to compare them easier with the MIPAS-ACE and MIPAS-SABER $CO_2$ differences.

## 6. Comparison of MIPAS $CO_2$ With ACE and SABER Measurements

The fact that ACE is an occultation instrument, with limited latitude and local solar time coverage (only at sunrise and sunset), and that MIPAS measured every about 10 days and always at 10 A.M. makes the number of coincidences rather limited. In order to maximize the number of coincidences, we have inspected ACE $CO_2$ data for possible local time (sunrise and sunset) dependencies. The ACE $CO_2$ sunset-sunrise differences are shown in Figures S1.1 and S1.3 in the supporting information, together with their latitudinal and daily coverages (Figures S1.2 and S1.4). We should note that ACE sunset and sunrise in those figures and in this work correspond to the "atmospheric" sunset and sunrise (i.e., those occurring at local times between 12 h and 24 h and between 0 h and 12 h, respectively), not to the "satellite" sunset and sunrise that are specified in the ACE data. Although both criteria generally coincide, there are some days of measurements in May, June, December, and January, where they are actually exchanged. Figures S1.1 and S1.3 show that above around 100 km there is a clear difference in the $CO_2$ vmr of about 20% between sunrise and sunset measurements, being larger at sunset. This might suggest, in principle, a local time dependency. However, the inspection of Figures S1.2 and S1.4 show that the sunset and sunrise measurements within a month at a given latitude are usually taken several weeks apart. It is then not clear if the differences in Figures S1.1 and S1.3 are caused by the local time variation or if they just reflect the temporal (seasonal) variation of $CO_2$. In order to further investigate this behavior, we looked at the ACE(sunset)-MIPAS and ACE(sunrise)-MIPAS differences for months and regions where we expect the local time to have a large (tidal) effect. October is a good month when the tidal amplitude is large and the equator and tropical latitudes are well covered by ACE. The results are shown in Figure S1.5 (see more details of the MIPAS/ACE coincidences below). We see that the ACE(SS, separated from MIPAS in about 8 h) — MIPAS differences (Figure S1.5, bottom left) present a recognizable tidal pattern. If comparing MIPAS with the ACE measurements taken at sunrise, separated from MIPAS by only about 4 h, we see that the differences are smaller, particularly above 105 km, and the tidal pattern is reduced. Thus, at least part of the differences in ACE(sunset)-ACE(sunrise) in Figures S1.1 and S1.3 seem to be caused by the different local times. As a consequence, we have taken for the comparison with MIPAS only sunrise ACE data, which are closer in local time to the MIPAS 10 A.M. measurements. Nevertheless, for completeness, the annual mean of the monthly zonal mean differences is also presented for sunset (see Figure 13).

In addition to the local time, given the limited number of days of MIPAS measurements on one hand and the expected seasonal variation of $CO_2$ on the other, we have taken a compromised temporal coincidence criteria of 3 days. The detailed comparison covers the period of January 2007 until December 2011, when MIPAS

was measuring in the UA mode more routinely. A further comparison at several altitudes for a near global coverage of 60°S–60°N along several years showing also the MIPAS data in 2005, 2006, and January–March 2012 is discussed in section 8.

About the coincidence criteria between MIPAS and SABER, we have taken only the data measured by both instruments on the same day and within a solar local time maximum difference of 4 h. We recall that only daytime measurements were taken by both instruments. The coincident data have then been binned in 10° latitude boxes, independently for each instrument. Widening/shortening the local time difference by 2 h leads to a larger/smaller latitudinal coverage of coincidences between both instruments. This is due to the nonglobal latitude coverage of SABER and the precession of its orbit, producing a local time variation along the yaw cycle of about 60 days. The change of the local time interval also produces changes in the $CO_2$ MIPAS-SABER differences on the order of 5% at some latitudes. Therefore, we assumed a local time interval of 4 h as a compromise between the latitudinal coverage of the coincidences and the potential systematic biases (e.g., tides) introduced by differences in the local time. Occasionally, e.g., for checking the differences at polar summer conditions in the Northern (NH) and Southern (SH) Hemispheres, we performed comparisons (as noted) with an increased local time interval of 6 h.

We have not included in the comparison the possible effects introduced by the different averaging kernels (AKs) of the three instruments. This is currently not possible because neither SABER nor ACE-FTS inversions provide routine AKs for the inverted $CO_2$ data. Nevertheless, we expect this effect not to be very important since the three instruments have very similar vertical resolutions in the region of comparison (see previous sections).

The comparison is organized according to seasons, equinox (months of March and September) first and solstice conditions (months of June and December) later. Before showing the differences of the instruments for the coincident data, we present the zonal mean distribution of $CO_2$ vmr of the three instruments as they measure the atmosphere with their respective coverages (not coincidences) (see Figures 1 and 2). They have been computed by averaging all the data available for all longitudes at the given month for 10° latitude bins and a vertical grid of 2 km. Similar plots for all months are shown in Figures S2.1–S2.6 in the supporting information. Similarities and differences in major patterns can be appreciated. For example, the $CO_2$ fields at equinox from the three instruments are quasi-independent of latitude (see Figure 1), although SABER seems to show significant meridional gradients below about 100 km near the northern polar region in March and the southern polar region in September. The limited coverage of ACE is reflected in the lack of measurements at tropical and middle latitudes in these months. Further, the sampling (the two latitudinal bands in each month correspond to different local times, sunrise (SR) in the SH and sunset (SS) in the NH in March, and the opposite in September) seems to introduce discontinuities in the $CO_2$ fields (see, e.g., Figure 1, middle row, left). MIPAS data (and also SABER, although to a much lesser extent) seem to show a typical diurnal tidal feature at 90 to 100 km at the equator, with corresponding out of phase signatures around ±30°, which is present in March (strongest) and September. In that altitude region there is an apparent downwelling near the equator and upwelling at subtropical latitudes. For solstice (see Figure 2), the three instruments show the typical zonal mean pattern of $CO_2$, mainly driven by the meridional circulation, with concentrated $CO_2$ isolines (centered around 90–100 km) near the summer pole (upwelling air from below near 90–95 km and descending air from above) and diverging isolines in the polar winter (descending air from 90 to 95 km to lower heights and ascending air to the regions above) [see, e.g., *Smith et al.*, 2011]. MIPAS data show also the tidal feature for solstice conditions but weaker than during equinox. MIPAS $CO_2$ vmr also shows a significant increase near 30–40°N in June and at 30–40°S in December at 100–120 km. The feature is also present in the MIPAS $CO_2$ density and in the temperature (not shown). Although we have no clear explanation for it, it might also be produced by the diurnal migrating or another tidal mode (even semidiurnal).

Figures 3–5 show the comparison of MIPAS $CO_2$ abundances coincident with those measured by ACE and SABER for equinox conditions (March and September). Similar figures for all months are shown in Figures S3.1–S3.4 in the supporting information. Figures 4 and 5 (an those corresponding to solstice conditions, Figures 7 and 8) also show the WACCM simulations sampled at MIPAS geolocations, but these are discussed later in section 7. We see in Figure 3 (top row) an overall very good agreement between MIPAS and ACE at altitudes below around 100 km, with differences limited to approximately ±5% for all latitudes.

At higher altitudes we find that ACE $CO_2$ is generally larger than MIPAS measurements with the differences growing with altitude and reaching values as large as 40–50% near 110–120 km. These rather large
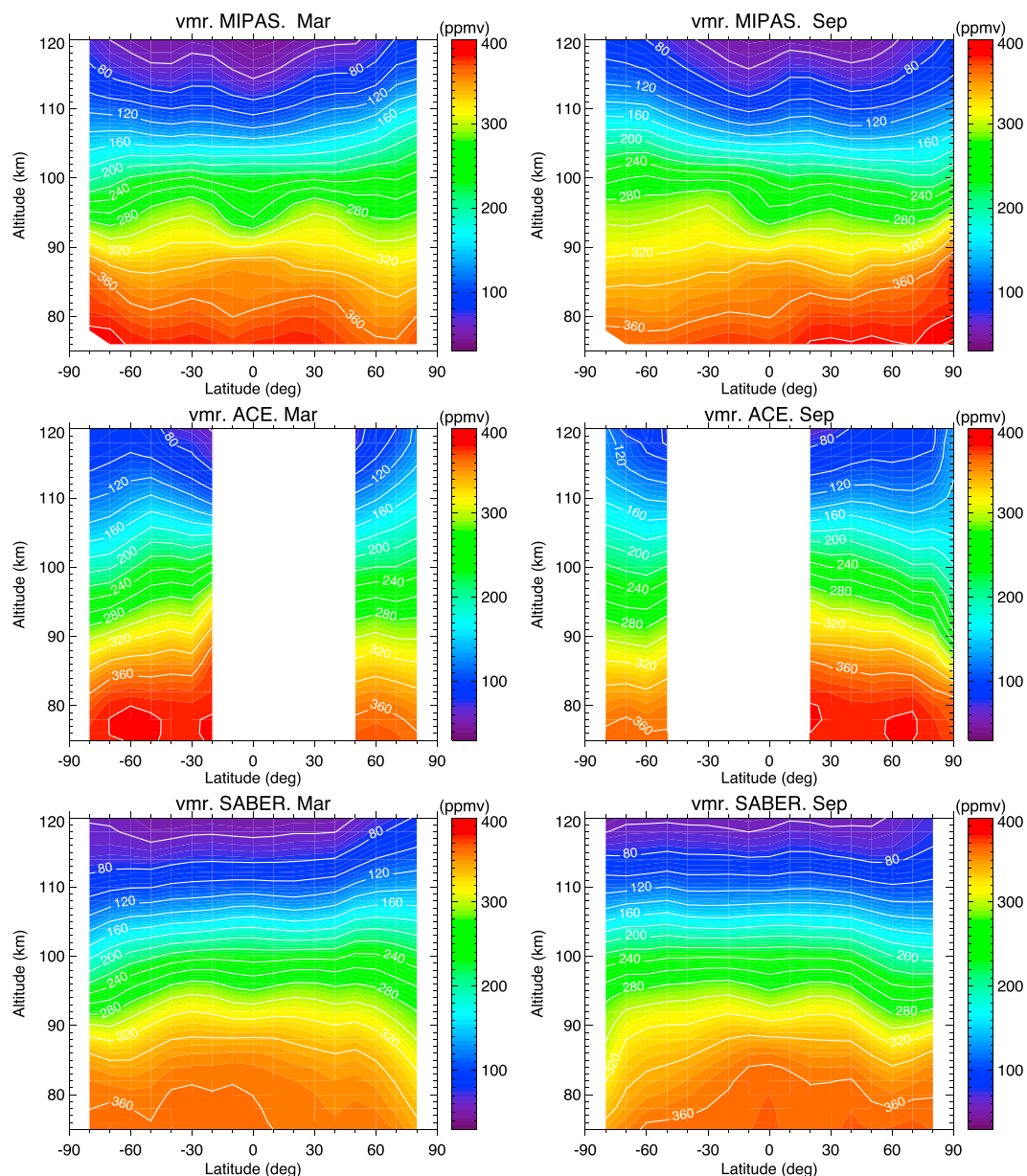
**Figure 1.** Zonal mean CO$_2$ vmr abundances for (left column) March and (right column) September of (top row) MIPAS, (middle row) ACE, and (bottom row) SABER for the period of 2007–2011. No coincidence criteria were used here. ACE data include both sunrise (SR) (SH in March and NH in September) and sunset (SS) (NH in March and SH in September).

differences above ~110 km are also clearly shown in Figure 4, illustrating that they are larger than their combined errors. Differences for March and September at these altitudes are very similar.

Absorption-based studies with CO$_2$ transitions limited to the ground vibration in the lower state are often perceived as being insensitive to non-LTE effects. However, large-scale effects in the population distribution above 100 km from non-LTE processes, as described in *Edwards et al.* [1998], will have an impact even in absorption-based studies, and accurate determination of CO$_2$ amounts above 100 km requires taking this into account. In particular, *Edwards et al.* [1998] reported that the non-LTE effect in the CO$_2$ vibrational partition function grows quickly with altitude above 100 km, being as large as 50% at 140 km. This non-LTE effect is mainly induced by the non-LTE population of the CO$_2$(010) state, which is much less populated than in LTE and hence causes the ground state to be more populated. Nevertheless, no non-LTE correction was applied
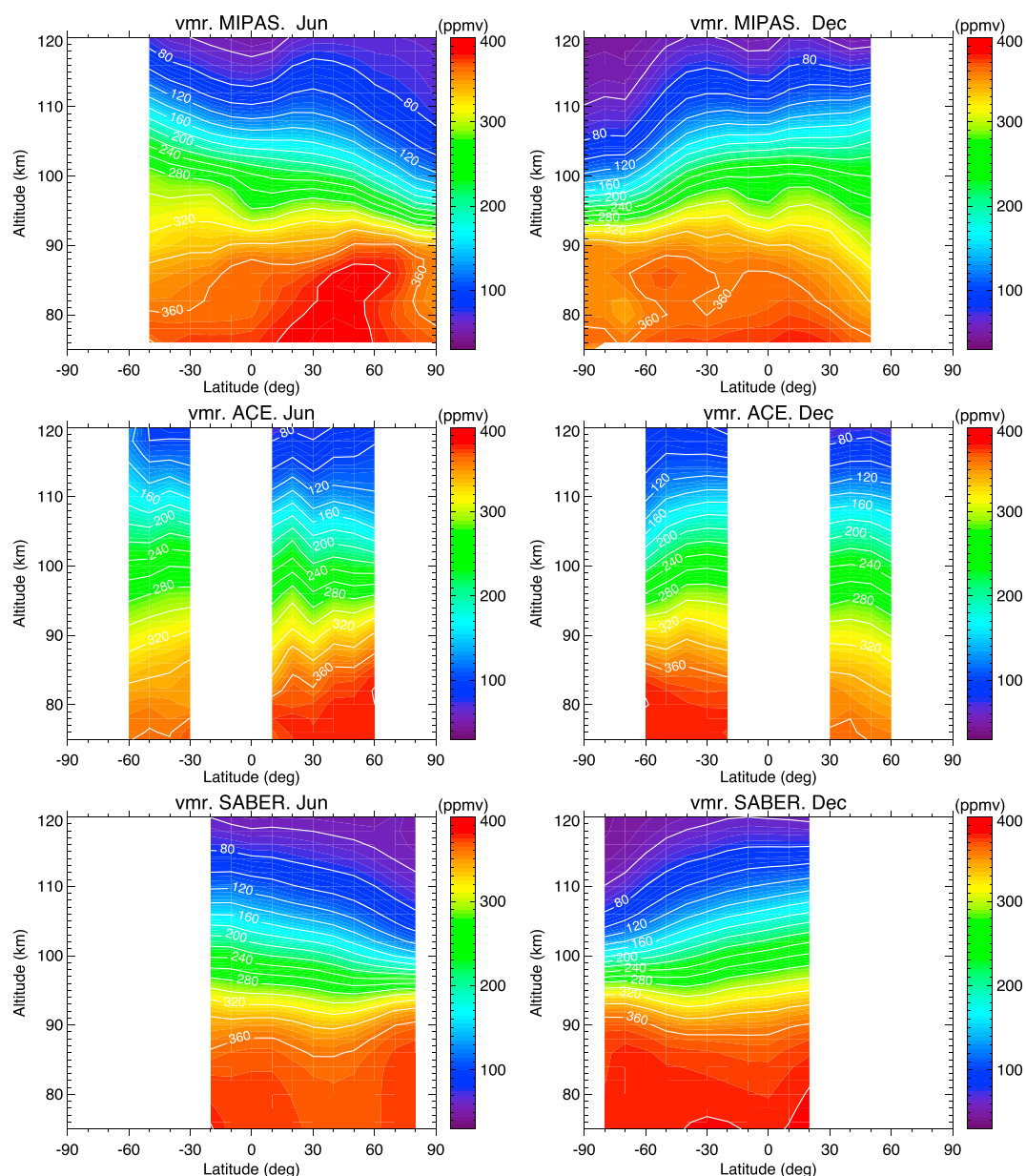
**Figure 2.** As Figure 1 but for (left column) June and (right column) December.

to ACE data. We have estimated this effect by using the simple formula for the ratio of the vibrational partition function of

$$\frac{Q_v^{NLTE}}{Q_v^{LTE}} \approx \left[\frac{1 - \exp(-E_v/kT_k)}{1 - \exp(-E_v/kT_v)}\right]^2, \tag{1}$$

where $k$ is Boltzmann's constant and $E_v$ is the vibrational energy of $CO_2(010)$ and the approximation for the vibrational temperature of $CO_2(010)$, $T_v$, given by equation (2) of *López-Puertas et al.* [1992]. Using the kinetic temperature $T_k$ measured by ACE, we have found that this correction would reduce the retrieved ACE $CO_2$ by about 5% at 110 km and in the range of 10–15% at 120 km, which would then partially explain the differences with MIPAS (and also with SABER, see below).

The comparison with SABER (Figures 3 (middle row) and 5) shows that below about 100 km, SABER–MIPAS $CO_2$ differences are within ±5% with a general tendency of SABER being larger than MIPAS around the equator. Between 100 and 120 km, SABER tends to be larger (10%) around the equator and tropics and smaller
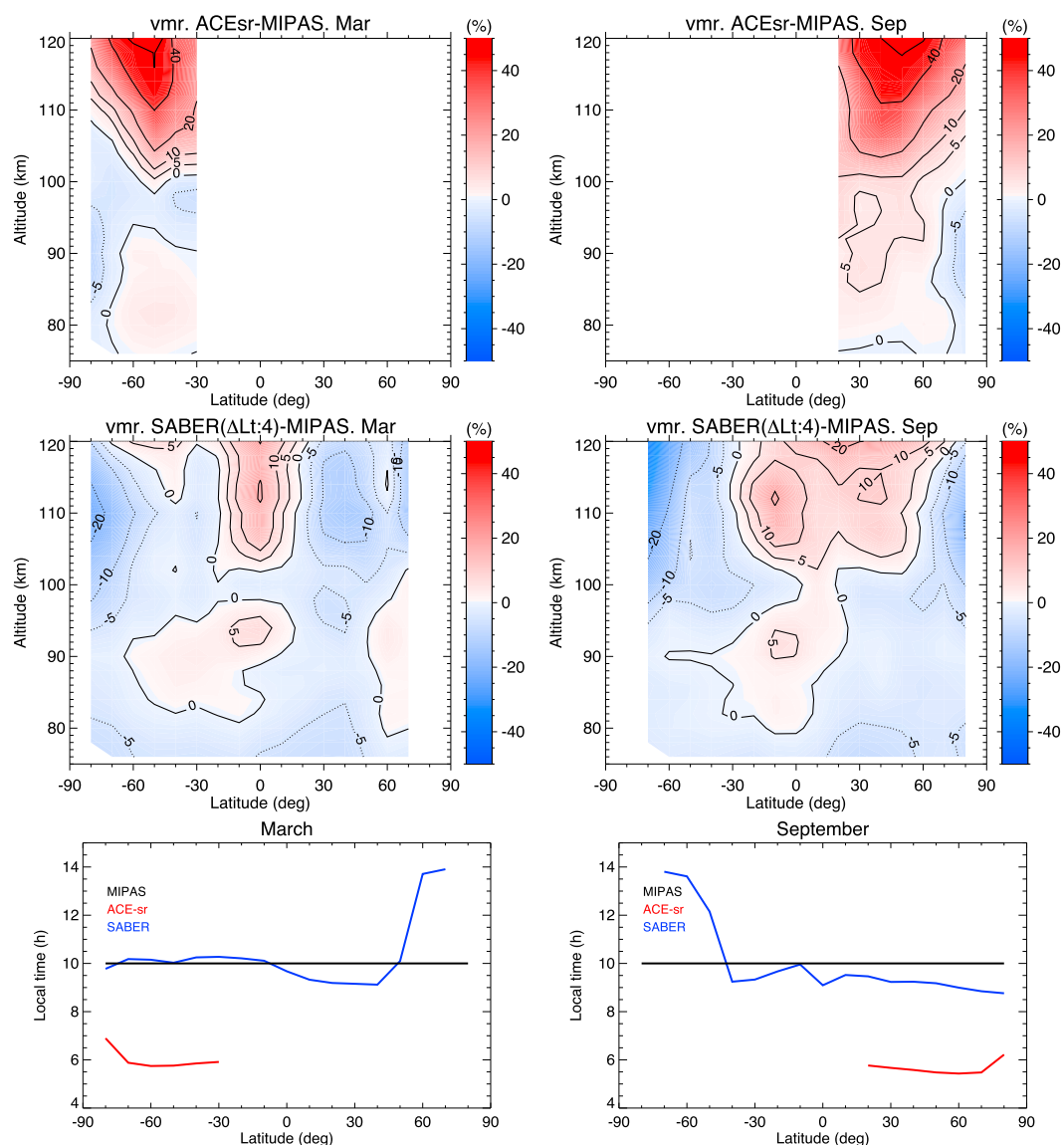
**Figure 3.** Zonal mean of the $CO_2$ vmr relative differences of (top row) ACE and (middle row) SABER with respect to MIPAS (in % of MIPAS) for (left column) March and (right column) September. (bottom row) The local times of the three instruments.

($\sim$10%) near the polar regions. That is, the two instruments show a different tropic-to-poles latitudinal gradient at these higher altitudes. We should note that the larger differences up to $-20\%$, occurring near 60°S in September, correspond to coincidences with local time differences larger than 2 h (see Figure 3 (bottom right)). So it is likely that these larger differences might be partially due to the relatively large local time mismatch. By looking at Figure 1 one notes that this difference is caused by the different latitudinal gradient in this region, being SABER $CO_2$ very flat but MIPAS, as well as ACE, is increasing toward the South Pole. It is also noticeable that the differences between MIPAS and SABER $CO_2$ measurements are significantly smaller than their combined errors, dominated by the larger SABER errors, for all latitudes and altitudes in equinox conditions (see Figure 5). This suggests that SABER $CO_2$ systematic errors have been overestimated or that MIPAS and SABER are affected by the same systematic errors.

In solstice conditions, the agreement of MIPAS with ACE (Figures 6 (top row) and 7) below about 100 km is similar to that for equinox conditions. However, around 85–90 km at midlatitudes in the summer hemisphere, ACE is smaller by a few percent ($\leq$5%), while it is generally larger by 5% in equinox. Above 100 km, we also
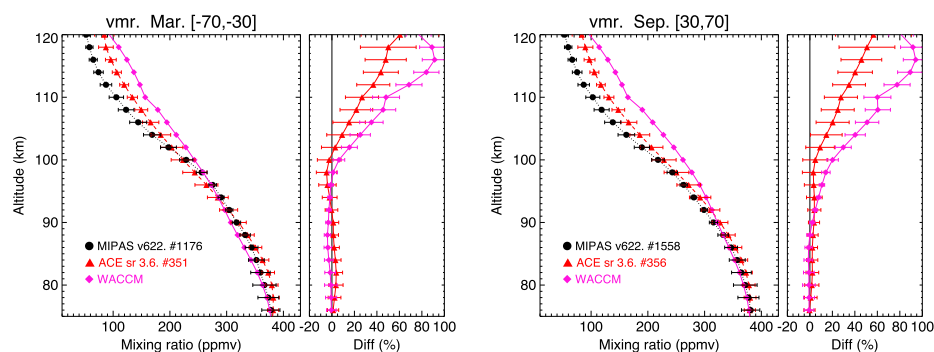
**Figure 4.** $CO_2$ vmr profiles and differences of ACE and MIPAS corresponding to the two latitude bands of ACE measurements for (left) March and (right) September. Horizontal bars in the $CO_2$ vmr profiles are the total errors of the respective instruments, dominated by their systematic errors. The number of coincident profiles is also shown. Model WACCM profiles for the same latitude bands are also shown (magenta lines) and are discussed in section 7. The profile differences are plotted with respect to MIPAS in percent of MIPAS. The error bars in the differences are the combined errors of the two instruments. In the case of WACCM, the error bars are the MIPAS errors.

observe very similar patterns as for equinox, with MIPAS $CO_2$ generally smaller than ACE $CO_2$ in the range of 10–40%.

The agreement of MIPAS with SABER for solstice is generally good, although not as good as for equinox (see Figure 6 (middle row) and the vertical profiles in Figure 8). Below about 95 km the differences are of the same magnitude as for equinox, in the range of ±5%. We observe, however, that SABER $CO_2$ is generally smaller in June, while it is larger in December.
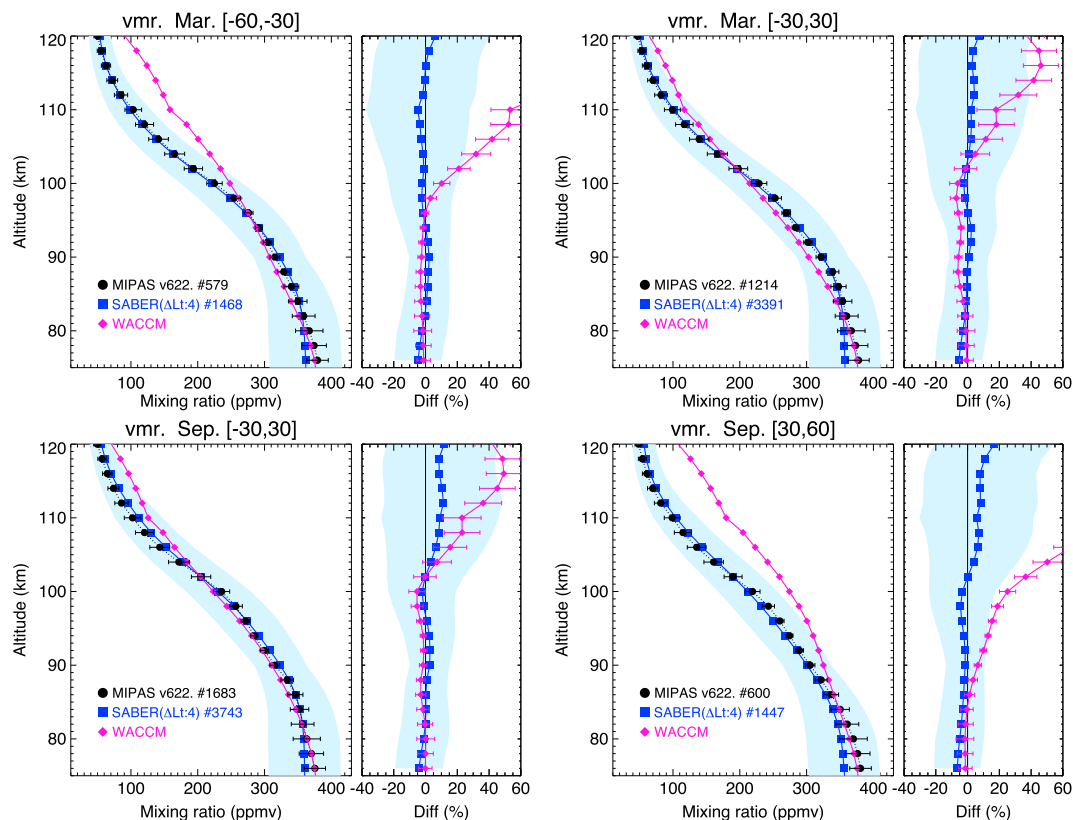


**Figure 5.** Similar to Figure 4 but for the SABER and MIPAS $CO_2$ vmrs. Note the different latitudinal bands profiles corresponding here to midlatitudes (30°–60°) and to the tropics (30°S–30°N). Note also that the combined errors of SABER and MIPAS (blue shaded areas) in the differences panels are mainly dominated by the SABER errors.
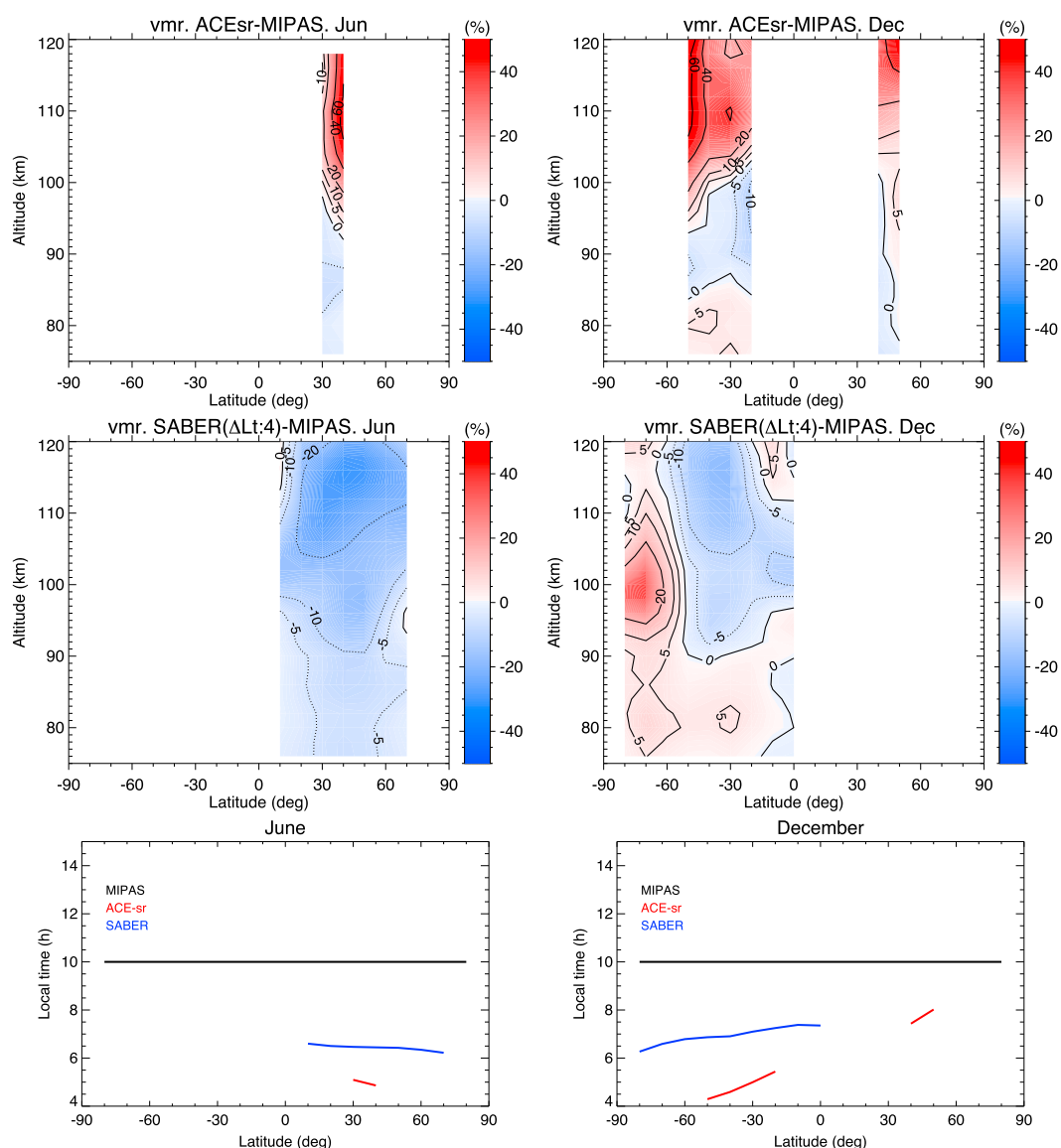
**Figure 6.** Zonal mean of the $CO_2$ vmr relative differences of (top row) ACE and (middle row) SABER with respect to MIPAS (in %) for (left column) June and (right column) December. (bottom) The local times of the three instruments.

In the southern polar summer region, below about 90 km (see Figure 8, bottom left), MIPAS $CO_2$ is smaller than SABER by about 5% and seems to be rather low. However, the comparison with SABER does not help much since its $CO_2$ has a poor vertical resolution in this region (just a single value is retrieved for the 65–90 km range) [see *Rezac et al.*, 2015a]. ACE did not cover latitudes beyond 60°S in the summer SH. However, ACE measurements taken close to the polar region are also larger than MIPAS but by less than 5%, and within the MIPAS and ACE combined errors (see Figure 7, right). Figure 2 (top row) reveal, however, that such low MIPAS values do not appear in the northern polar summer region. The retrieval of $CO_2$ in the polar summer region is very difficult because of the very cold temperatures and the large errors in the kinetic temperature and its coarse vertical resolution. In the case of MIPAS and SABER, which are emission instruments, we have additionally strong LOS gradients of the population of the excited emitting states combined with rather large solar zenith angles. Hence, the MIPAS $CO_2$ low values near the polar summer mesopause in the SH remain to be validated.

One of the largest differences between MIPAS and SABER are found near the southern polar summer regions at altitudes of 90–105 km, where SABER is generally larger by up to about 20–30% (see Figure 6 (middle row, right) and Figure 8 (bottom left)). These high values are, however, somehow expected as in this region $CO_2$
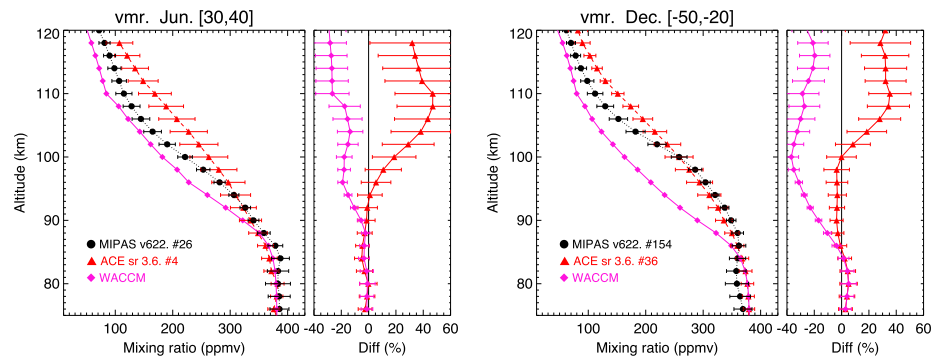
**Figure 7.** Similar to Figure 4 but for solstice conditions for latitudes of 30°N–40°N in (left) June and 50°S–20°S in (right) December.

vmr exhibits its largest gradient in the whole atmosphere (see also Figure 2). These differences, although are within the rather large errors for these conditions (see panels of Figure 8), appear to be systematic. A similar feature is found, but not so pronounced, for the polar summer in the NH, not covered in Figure 6 but visible when relaxing the local solar time criteria to 6 h (not shown).

At altitudes of 100–120 km, for solstice conditions, MIPAS $CO_2$ is generally larger than SABER in a range of 10 to 20%, except as noted above near the polar summer regions. These differences are more pronounced in June when MIPAS $CO_2$ exhibits a significant "prominence" in this region around 30°N (see in Figure 2 (top row, left)). A similar feature is observed in MIPAS temperatures (not shown) which hints that MIPAS is observing an atmospheric feature not present in SABER. Note that in the comparison of $CO_2$ number density (see Figure 10 below), for which the temperature effect through the atmospheric density should cancel, the differences are even more pronounced.
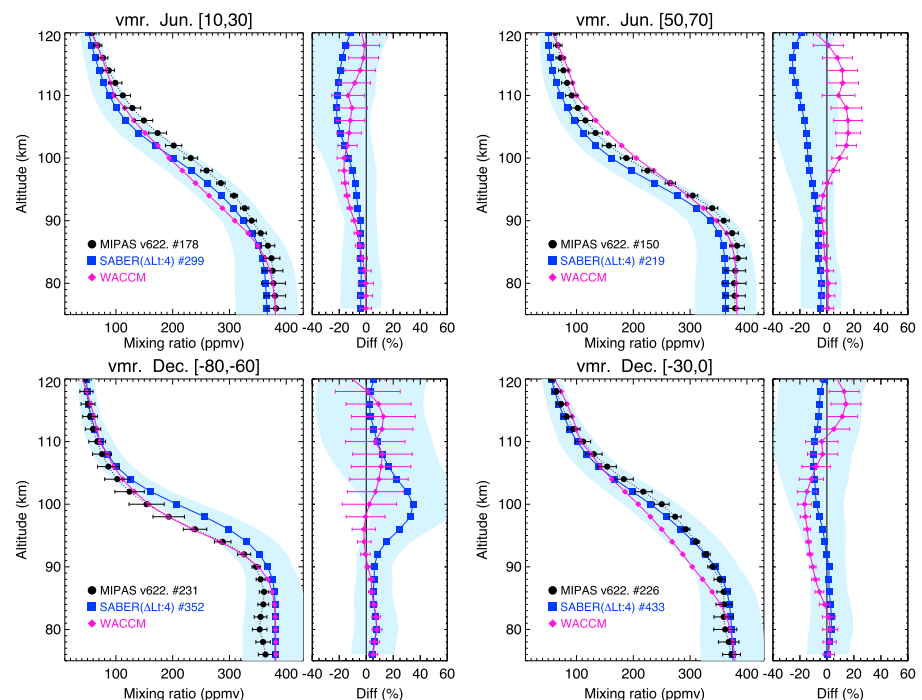


**Figure 8.** Similar to Figure 5 but for solstice conditions. Note the different latitudinal bands profiles corresponding here to near the tropics (10°N–30°N for June and 30°S–0 for December) and near the polar summer (50°N–70°N for June and 80°S–60°S for December). The combined errors of SABER and MIPAS (blue shaded areas) in the differences panels for these solstice conditions are rather larger because MIPAS errors for these conditions are also significantly large [*Jurado-Navarro et al.*, 2016].
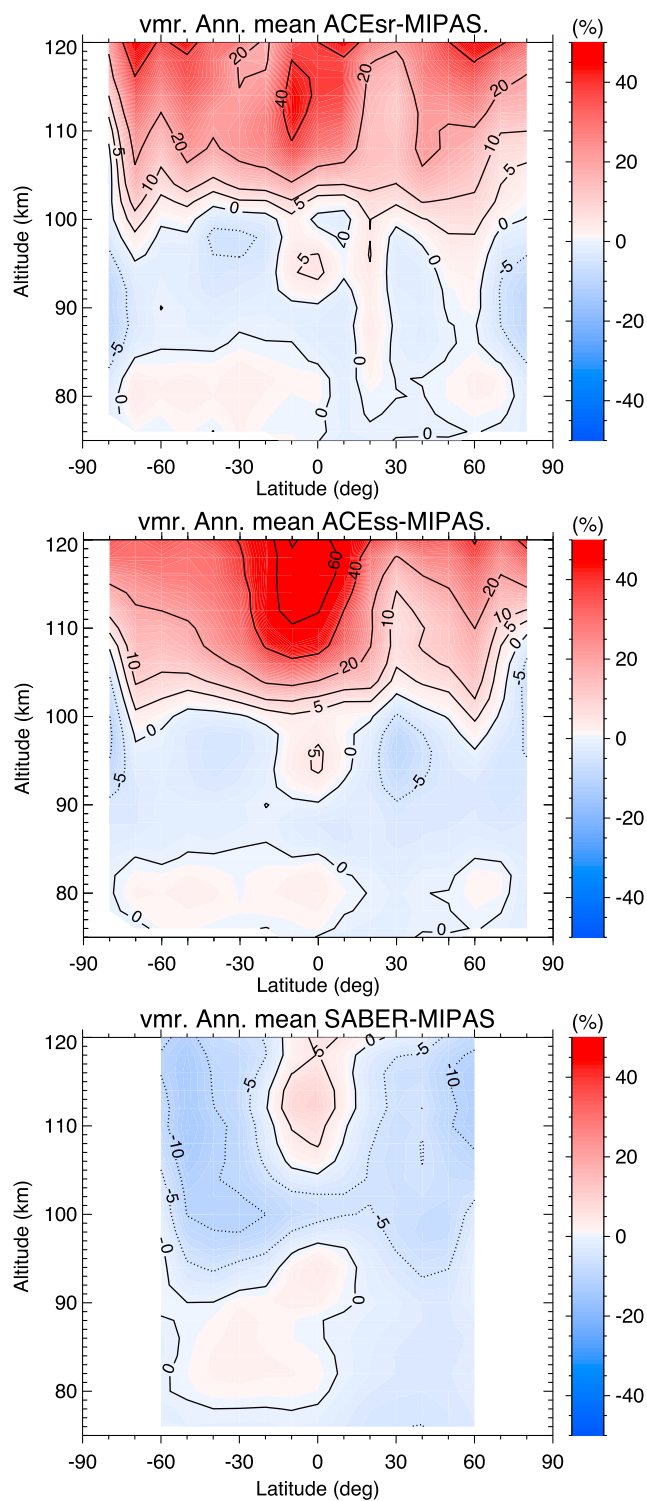
**Figure 9.** Annual mean of the (top) monthly zonal mean ACE(SR)-MIPAS differences (e.g., as in Figures 3 and 6), for (middle) ACE(SS)-MIPAS, and of the (bottom) SABER-MIPAS differences of the $CO_2$ vmr abundances for 2007–2011.
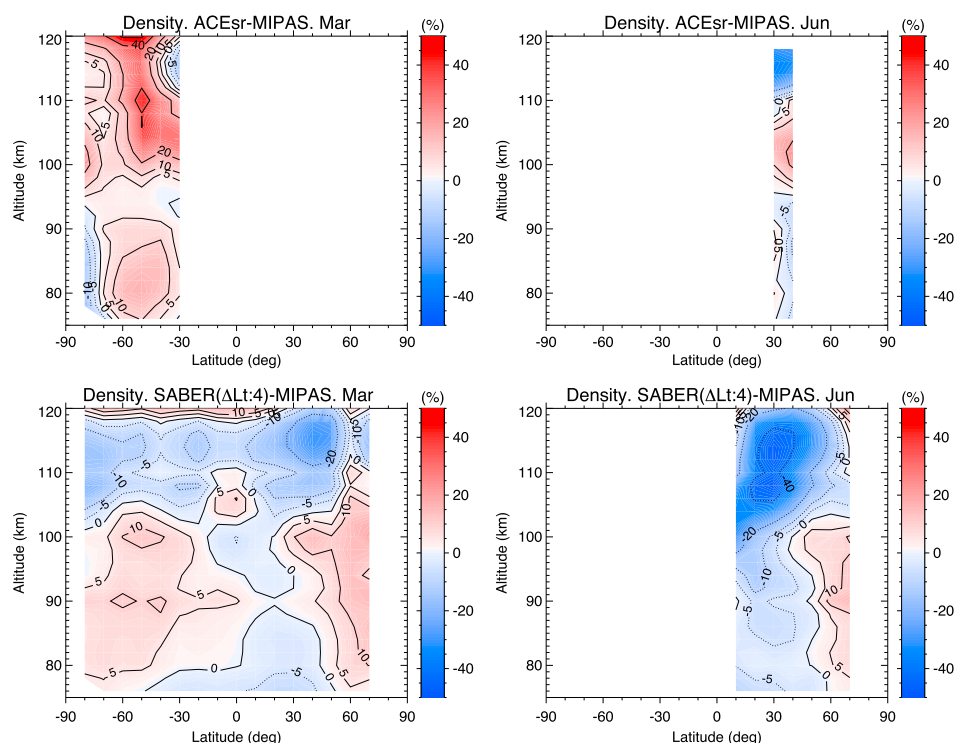
**Figure 10.** Zonal mean of the $CO_2$ density relative differences of ACE with respect to MIPAS (in percent of MIPAS) for (left column) March and (right column) June.

In order to have a global view of the differences, we show in Figure 9 the mean over all months of the ACE(SR)-MIPAS, ACE(SS)-MIPAS, and SABER-MIPAS zonal mean monthly differences. Note that for the SABER-MIPAS differences we have omitted the polar regions because the differences for the alternating sol-stice conditions along the different months would cancel out leading to misleading results. When comparing MIPAS with ACE(SR) (Figure 9, top), it is evident that MIPAS agrees very well with ACE (better than 5%) below 100 km. However, between 100 and 120 km, it is clear that ACE $CO_2$ is larger by 5 to 30% at all latitudes, except near the tropics where the differences are slightly larger, reaching 40%. It is also evident that the differences are larger for ACE sunset particularly at the equator and tropical latitudes above around 105 km. MIPAS and SABER also agree very well up to 100 km (within $\pm 5\%$). At 100–120 km, the agreement of MIPAS with SABER is better than with ACE. SABER $CO_2$ is higher than MIPAS near the equator by as much as 5% (Figure 9, bottom), but it is smaller by about 10% at the other latitudes. From this comparison it is clear that in the 100–120 km region, globally, ACE shows the highest $CO_2$ vmrs. Part of these differences ($\sim 10\%$) would be mitigated (see above) if including a non-LTE correction in the ACE $CO_2$ retrieval.

### 6.1. Comparison of $CO_2$ Number Density

Because the measured quantity by the three instruments is directly related to the $CO_2$ number density (not vmr) and the vmr might be affected by differences in their respective measured temperatures, we have also analyzed the differences in $CO_2$ number density. We show here the differences only for March and June (see Figure 10).

Focusing on March, comparing Figures 3 (left column) and 10 (left column), we generally see below about 95 km larger differences in $CO_2$ number density than in vmr, being about 10% for ACE-MIPAS and 5% for SABER-MIPAS. This is caused by the larger pressure retrieved in both ACE and SABER with respect to MIPAS. This change is actually rather small, since it can be explained by a difference of about 250–500 m in the pointing of the instruments, fully in-line with their errors. In the case of ACE, the exception at 80–90 km near the South Pole is noticeable, where ACE $CO_2$ densities are significantly smaller than MIPAS. This is induced by the 10 K warmer ACE temperatures in that region, also warmer than SABER temperatures (not shown). At altitudes around 95–110 km the ACE-MIPAS differences in $CO_2$ density are larger than in vmr because of the colder

ACE temperatures, and at 110–120 km they are reduced due to the smaller ACE pressures. The SABER-MIPAS differences in $CO_2$ density above about 100 km are generally smaller than in vmr, in large part caused by the warmer SABER temperatures.

For solstice, comparing Figure 6 (first column, top and middle) and Figure 10 (right column), similar effects of pressure and temperature differences apply, leading to a worst agreement (more evident in SABER) in $CO_2$ density than in vmr. The larger differences in $CO_2$ density below about 95 km for SABER are due to their larger pressures. The differences above that altitude are principally driven by the differences in temperature: ACE significantly cooler than MIPAS (∼20 K) around 100 km and warmer (∼40 K) at 110–120 km. The large SABER-MIPAS $CO_2$ density differences above 100 km in June are mainly caused by the very large SABER temperatures (∼20 K and ∼60 K larger than ACE and MIPAS, respectively). We should recall that SABER does not measure temperature in that region although this should not affect the retrieved $CO_2$ number density when expressed as function of geometric altitude.

## 7. Comparison of $CO_2$ MIPAS Data With WACCM Simulations

The chemistry of CO and $CO_2$ and the calculation of eddy diffusion have recently been updated in WACCM, and the model results have been compared to ACE CO and $CO_2$ measurements and MIPAS CO abundances [*Garcia et al.*, 2014]. Here we show a comparison of WACCM simulations with MIPAS $CO_2$. The rationale behind the comparison is to explore whether MIPAS data can give us any information about the dynamics and chemistry of the upper atmosphere with emphasis above 120 km, a region where MIPAS provides the first $CO_2$ vmr measurements. We should have in mind though that WACCM's upper boundary is close to 140 km ($6 \times 10^{-6}$ hPa). Hence, differences in $CO_2$ at altitudes below 1–2 scale heights of the upper lid might be affected by the fixed conditions imposed there.

We used WACCM calculations sampled at the MIPAS geolocations and times for the 2007–2011 period. As discussed above, the comparison was performed on the native WACCM vertical coordinate, e.g., pressure $p$, although the plotting was done on geometric altitude $z$ by using the MIPAS-derived $p(z)$ for each profile. The comparison is carried out with two WACCM simulations, one using the current standard Prandtl number of $Pr = 2$ and another using a larger value of $Pr = 4$, which is equivalent to decreasing the eddy diffusion coefficient $k_{zz}$ by a factor of 2. The results are shown for equinox (March) and solstice (June) conditions (see Figures 11 and 12). Similar plots for all months are shown in Figures S4.1–S4.12 in the supporting information. $CO_2$ profiles of standard WACCM simulations for several latitudinal bands are also shown above in Figures 4, 5, 7, and 8 which are discussed here.

In general, the WACCM $CO_2$ shows the major features observed by MIPAS, in particular, its abrupt decline above 80–90 km and the seasonal change of the latitudinal distribution, with higher $CO_2$ abundances from 70 km up to ∼95 km in polar summer and lower $CO_2$ vmr in the polar winter. Above ∼95 km, the $CO_2$ vmr at a given altitude level is more abundant in the polar winter than at midlatitudes and polar summer regions, caused by the reversal of the meridional circulation in that altitude region.

More specifically, in the region of 80–100 km the agreement is very good for equinox conditions, within ±5%, at all latitudes (see Figures 11, 4, and 5). However, a small underestimation of $CO_2$ (∼5%) by WACCM with respect to MIPAS can be appreciated in the tropics. The same happens for ACE and for SABER, for which differences are slightly larger. This means that the decline with altitude of $CO_2$ near the homopause is slightly stronger in the model than in the measurements. For other equinox months, e.g., September (see Figure S4.9 in the supporting information), the differences in the 80–100 km range can be as large as ±10%, with a significant latitudinal dependence. We should note also that increasing the Prandtl number to $Pr = 4$ would worsen the agreement at these altitudes, hence suggesting that $Pr = 2$ gives a better representation of the atmosphere. For solstice conditions, e.g., June (see Figure 12), the differences below about 90 km are also very small (∼5%) but at 90–110 km they are larger, with WACCM underestimating MIPAS $CO_2$ in the range of 10–30% at most latitudes except near the polar summer where WACCM $CO_2$ is larger than MIPAS in about 20–40%.

At altitudes above 95–100 km WACCM significantly overestimate MIPAS $CO_2$ (40–80%) (and also SABER) for equinox conditions (March) (see Figures 11, 4, and 5). For other equinox months this overestimation is also present, although at some latitudes the differences are limited to ±20%, e.g., in the SH in September and October (see Figures S4.9 and S4.10 in the supporting information). For solstice conditions (June) the agreement is better and such overestimation above ∼100 km is not present. Differences are in the range of ±20%,

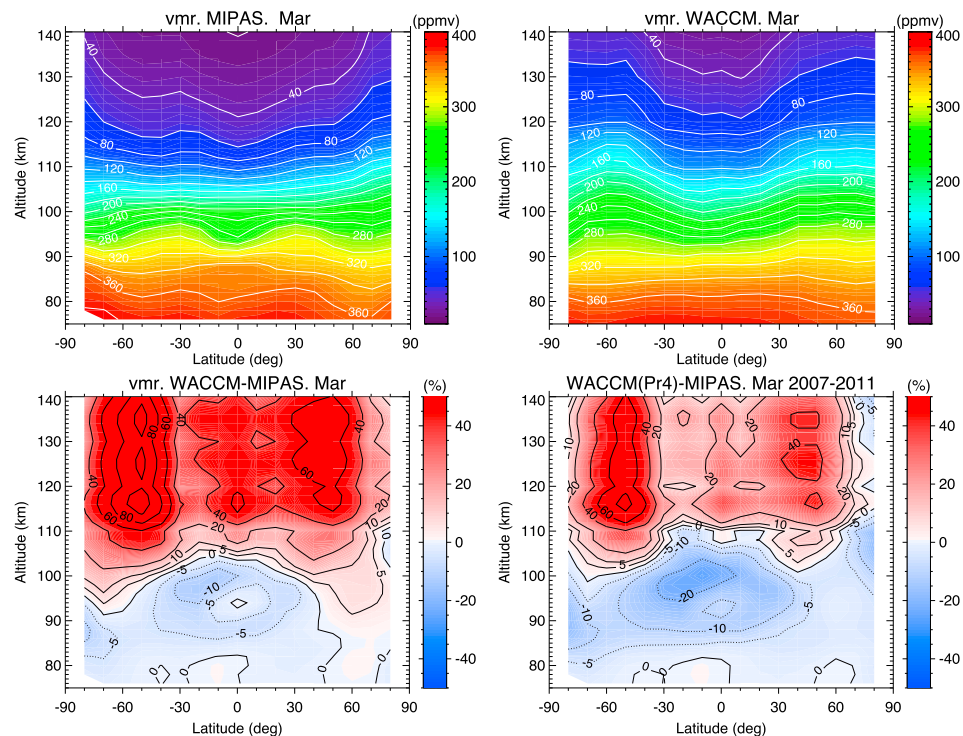**Figure 11.** Comparison of $CO_2$ vmr of MIPAS with WACCM for $Pr = 2$ and $Pr = 4$ for March. (top row) MIPAS (left) and standard WACCM (right) $CO_2$ vmr distributions. (bottom row) WACCM−MIPAS differences (in percent of MIPAS) for the standard $Pr = 2$ and the test $Pr = 4$, respectively.
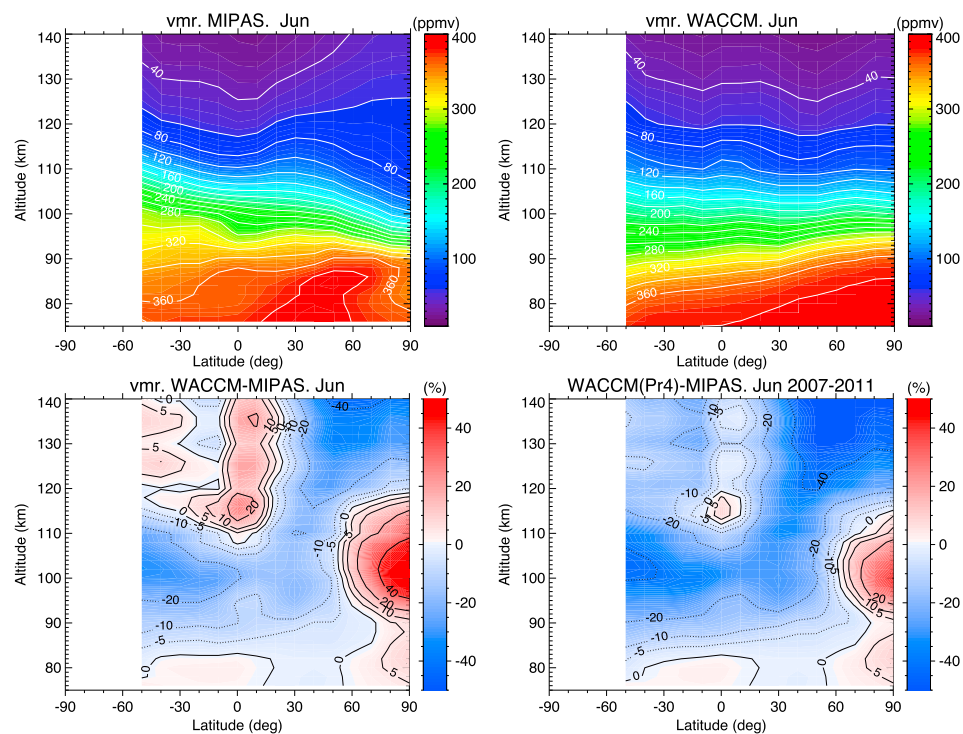


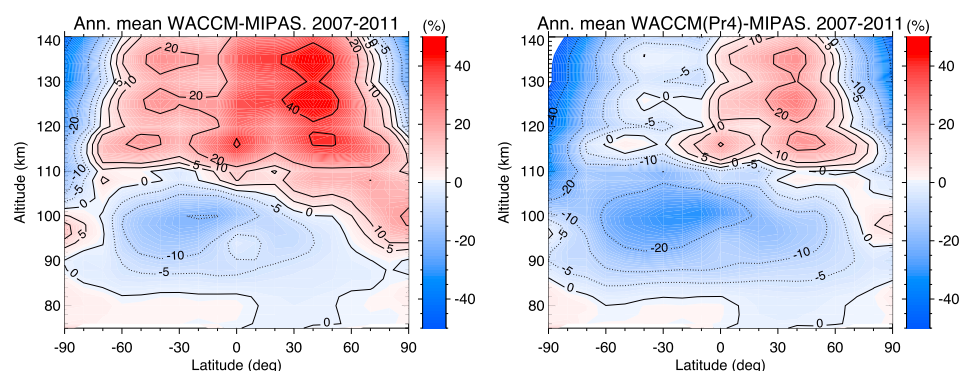**Figure 12.** As Figure 11 but for June.

**Figure 13.** Annual mean of the monthly zonal mean of WACCM-MIPAS $CO_2$ vmr differences for (left) WACCM-$Pr = 2$ and (right) WACCM-$Pr = 4$. The differences are plotted as percent of MIPAS.

with WACCM overestimating MIPAS $CO_2$ by only 5–20% at 50°S–20°N and underestimating it at polar summer latitudes (30°N–90°N). Similar patterns appear in December but reversed in latitude (see Figure S4.12 in the supporting information).

The WACCM overestimation at high altitudes in March could be due to an underestimation of the $CO_2$ photolysis, because WACCM has a very coarse parameterization of photolysis at short wavelengths [*Garcia et al.*, 2014]. However, the overestimation does not happen at all latitudes at other equinox months, such as September and October. Also, in June, we would expect a larger overestimation in the polar summer latitudes (longer illumination) but we see a WACCM underestimation there. It is true though that when considering the annual mean of the monthly differences (see Figure 13, left), we note an overall overestimation by WACCM. Thus, the $CO_2$ photolysis is probably underestimated in WACCM but this alone cannot explain all the differences.

The simulation of WACCM using $Pr = 4$, which is equivalent to globally reducing the eddy diffusion coefficient by a factor of 2, shows a general reduction of the $CO_2$ concentration at all latitudes and altitudes above around 80 km (see Figure 13). As was already found by *Garcia et al.* [2014] for ACE CO and $CO_2$ and MIPAS CO, we see here that the diffusion coefficient corresponding to $Pr = 2$ gives also a better overall agreement between WACCM and MIPAS below ~100 km (note also that as in *Garcia et al.* [2014], at high latitudes the agreement is also better for $Pr = 4$). At higher altitudes the simulations with the reduced eddy diffusion ($Pr = 4$) gives a better overall agreement (Figure 13, right). But it is not clear if this process is responsible for the differences or the $CO_2$ photolysis plays a more important role.

The $CO_2$ zonal mean fields of WACCM and MIPAS (Figures 11 (top row) and 12 (top row)) show some structures that seem more likely attributed to dynamical processes. For example, for March at 90–100 km, MIPAS shows a stronger tidal structure than WACCM. Also, above ~100 km, the kind of ascending branches in WACCM near ±60° is not present in MIPAS, and the increase of $CO_2$ near the poles in MIPAS is not present in WACCM fields. Likewise, near 90–110 km in the polar summer region in June, the $CO_2$ isolines are closer and lower in MIPAS than in WACCM. This suggests that the meridional circulation, with ascending air from below and descending from above, is stronger in MIPAS than in WACCM.

## 8. Time Series

We discuss in this section time series of the $CO_2$ measured by MIPAS, ACE, and SABER measurements and WACCM model simulations at several altitudes from 90 to 130 km and the near global latitude range of 60°S to 60°N. This is useful not only for studying the $CO_2$ midterm variability but also to extend the comparison of the three instruments and the WACCM simulations presented above to several years, covering the complete MIPAS period. The measurements and model simulations shown in this section include their respective global data, e.g., not only the coincident data.

Focusing on the intercomparison of the measurements and simulations, we observe in Figure 14 the main features we have described above. Thus, at 90 km, SABER measures the larger $CO_2$ vmrs, ACE $CO_2$ is slightly smaller, and MIPAS is essentially in between. We also see that ACE and MIPAS agree very well in the final period
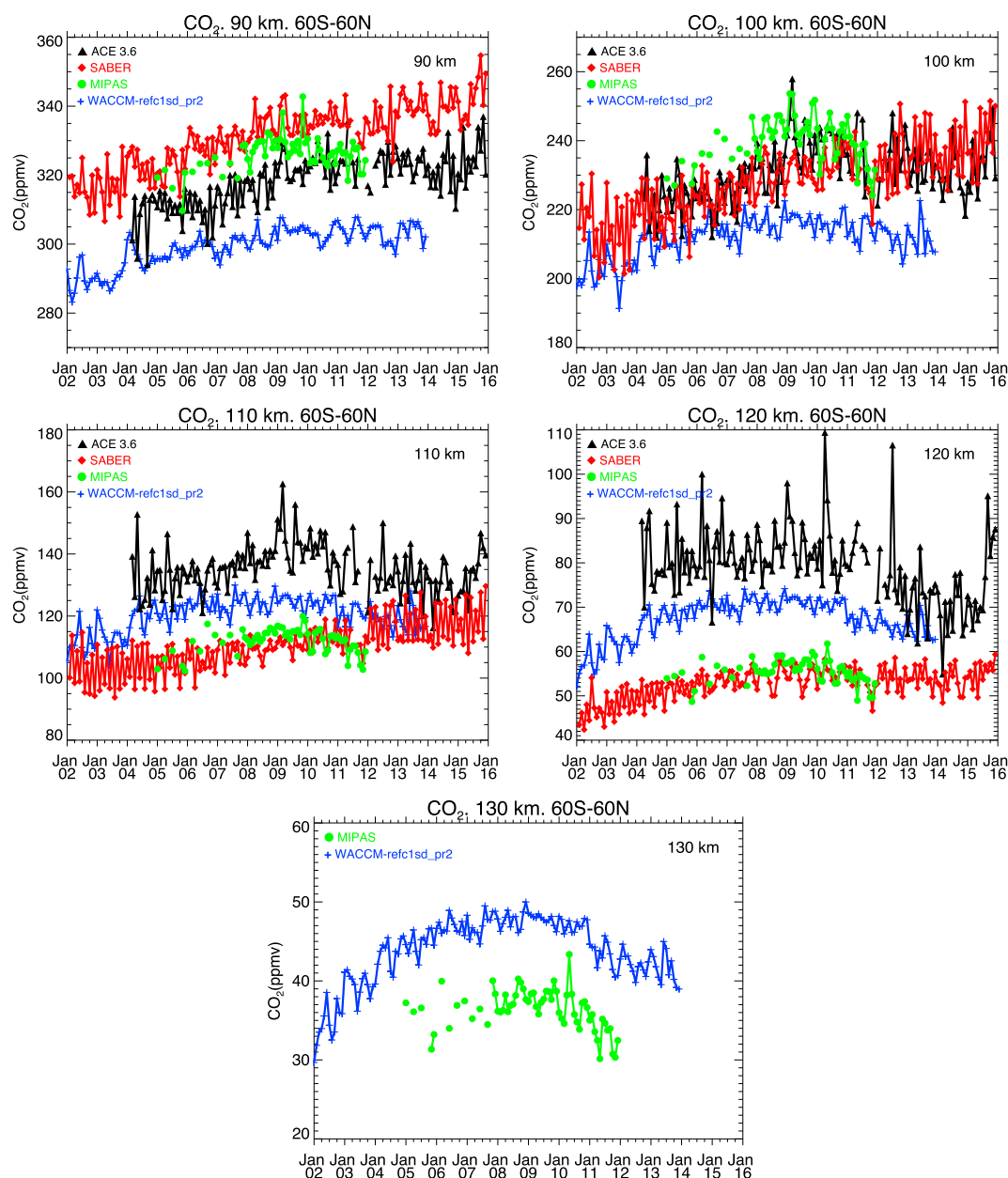
**Figure 14.** Deseasonalized monthly mean time series of ACE, SABER, MIPAS, and WACCM (*Pr* = 2) for the near global latitude coverage of 60°S–60°N at several altitudes, as labeled.

of MIPAS measurements in 2010–2011 but MIPAS is slightly larger in previous years. WACCM underpredicts, although not by a large amount, the three $CO_2$ data sets, essentially because the dropoff of $CO_2$ starts at lower altitudes than in the measurements.

At 100 km, the measurements of ACE, SABER, and MIPAS agree very well, and the agreement of the three instruments with WACCM is also better. At 110 km we note that ACE measurements are larger than SABER and MIPAS, while the latter two agree very well. At this altitude WACCM simulations are smaller than ACE but larger than SABER and MIPAS. At 120 km we observe the features discussed in previous sections, i.e., SABER and MIPAS agree very well but ACE $CO_2$ is significantly larger. WACCM simulations are within the observational spread, larger than SABER and MIPAS but smaller than ACE.

The fact that ACE is larger than both MIPAS and SABER above ~110 km can be partially explained by the fact that ACE lacks of a non-LTE correction, which is estimated in about 10–15% (see above). We do not expect

that the remaining differences are caused by a deficiency in the non-LTE modeling of $CO_2$ 4.3 μm in MIPAS and SABER because, if affected by an unknown non-LTE excitation, the non-LTE populations would be larger, resulting in even smaller MIPAS and SABER $CO_2$ abundances. It is noticeable, however, the fact that while ACE and SABER differences at 110 and 120 km are rather significant in the period studied here of 2007–2010, they tend to be negligible from 2011 to 2015. In particular, SABER does not show the expected decrease due to the rise of the solar activity. We have no explanation for this. At 130 km, WACCM and MIPAS show the bias already discussed above but have very similar time evolution, consistent with the lower altitudes.

In addition to the intercomparison, Figure 14 also shows an increase with time of the $CO_2$ vmr, mainly at lower altitudes where it is less affected by the solar cycle. That increase is visible in the three measurements and in the simulations. The effect of the solar cycle is also noticeable, producing a small relative maximum in $CO_2$ near the solar minimum, around 2008–2009, caused by the smaller EUV photodissociation. The maximum is more clearly seen at the highest altitudes in ACE and MIPAS data, while it is less distinguishable in SABER. WACCM simulations also exhibit this effect. The solar cycle signal and the trend in ACE $CO_x$ ($CO + CO_2$) have been studied in detail by *Emmert et al.* [2012] and also by *Garcia et al.* [2016] who additionally compared them with WACCM simulations. In a similar manner *Yue et al.* [2015] have analyzed the solar cycle and trend in $CO_2$ SABER data. A combined analysis of the trends and solar cycle signals in these three $CO_2$ data sets is, however, beyond the scope of this paper.

## 9. Summary and Conclusions

We have compared the $CO_2$ vmr global distributions measured by MIPAS, ACE, and SABER. The most important results are listed in Table 1 and summarized below. In order to reduce the impact of local time variations related to tides, the comparison of MIPAS data (taken at fixed local time of 10 A.M.) has been restricted to ACE sunrise occultations and SABER measurements taken at local times between 8 A.M. and 2 P.M. The three instruments show the major general features of $CO_2$ vmr predicted by models, i.e., (1) the abrupt decline of the $CO_2$ vmr above 80–90 km, predominantly caused by diffusive separation; (2) a nearly latitude-independent $CO_2$ field at 80–120 km during equinox; and (3) the typical $CO_2$ solstice pattern mainly driven by the meridional circulation with concentrated $CO_2$ vmr isolines around 90–100 km near the summer pole (produced by the ascending branch from below and descending branch from above) and diverged isolines (reversed branches) in the polar winter [see, e.g., *Smith et al.*, 2011].

In equinox, MIPAS shows an overall very good agreement with ACE at altitudes below around 100 km, with differences comprised within ±5% for most latitudes. Above 100 km, MIPAS $CO_2$ is generally smaller than ACE measurements with the differences growing with altitude and reaching values as large as 40–50% near 110–120 km. Part of this disagreement can be explained by the lack of a non-LTE correction in ACE data that would reduce the differences by 5% at 110 km and by 10–15% near 120 km. The agreement of MIPAS with SABER for these conditions is very good below about 100 km, with $CO_2$ differences within ±5% and a general tendency of MIPAS being smaller than SABER near the tropics. Between 100 and 120 km, SABER tends to be larger (10%) near the tropics and smaller (~10%) near the polar regions. Those differences are significantly smaller than their combined errors, dominated by the SABER errors, suggesting that SABER errors might have been overestimated. MIPAS data seem to show tidal signatures near the tropics in the 90–100 km region not so evident in SABER.

In solstice conditions, the agreement of MIPAS with ACE is also very good (±5%) below about 100 km. Around 85–90 km at midlatitudes in the summer hemisphere MIPAS $CO_2$ is larger than ACE in about 5%. Above 100 km, we observe very similar patterns than for equinox, with MIPAS $CO_2$ generally smaller than ACE $CO_2$ in the range of 20–40%. The agreement of MIPAS with SABER below about 95 km for these conditions is generally good (±5%) but not as good as for equinox. In this region, SABER is generally smaller in June while it is larger in December.

In the southern polar summer region, below about 90 km, MIPAS $CO_2$ is smaller than SABER in about 5% and seems to be rather low. The retrieval of SABER $CO_2$ there has a reduced vertical resolution and is not useful for validation purposes. ACE did not cover these high polar summer latitudes, but measurements taken close to the polar region are only slightly larger than MIPAS and within the MIPAS/ACE combined errors. Such low MIPAS $CO_2$ values do not appear, however, in the northern summer hemisphere. The inversion of $CO_2$ from 4.3 μm limb emission instruments in those atmospheric conditions is very difficult and, hence, the MIPAS $CO_2$ low values near the polar summer mesopause still remain to be satisfactory validated.

**Table 1.** Summary of the ACE and SABER $CO_2$ VMR Differences With Respect to MIPAS (in Percent of MIPAS, See Figures 3 and 6)

| Instrument | Altitude (km) | Equinox | | | Solstice | |
|---|---|---|---|---|---|---|
| | | Equator-Tropics | Middle Latitude | Polar | Equator-Middle Latitude | Polar Summer |
| ACE | 75–100 | 0–5 | 0–5 | 0,–5 | ±5 | NA |
| | 100–110 | 5–20 | 5–20 | 5–10 | 20–40 | NA |
| | 110–120 | 20–40 | 20–40 | 10–20 | 40 | NA |
| SABER | 75–90 | 0–5 | 0–5 | 0, and −5 | ±5 | ±5 |
| | 90–105 | 5 | 5 | −5 and −10 | −5 and −10 | 10–25 |
| | 105–120 | 10 | ±5 | −10 and −20 | −10 and −25 | 0–5 |

[a]NA: not available.

Significant differences between MIPAS and SABER are found near the southern polar summer regions at altitudes of 90–105 km, where SABER is generally larger by about 20–30%. The corresponding differences in the polar summer of the NH are smaller, ~10%. At altitudes of 105–120 km, for solstice conditions, MIPAS $CO_2$ is generally larger than SABER by 10 to 25%, except near the polar summer regions, where they are very similar (±5%).

WACCM $CO_2$ shows the major features measured by MIPAS, in particular, its abrupt decline above 80–90 km and the seasonal change of the latitudinal distribution. In the lower region, at 75–100 km, the agreement is generally very good (±5%) for almost all latitudes of the equinox season. For some months/latitudes the maximum differences can be as much as ±10%. WACCM simulations, however, slightly underestimate (~5%) MIPAS $CO_2$ systematically (also for SABER and ACE) near the tropics. That is, the decline with altitude of $CO_2$ near the homopause is slightly stronger in the model than in the measurements. For solstice conditions, the differences below about 90 km are also very small (~5%) but at 90–110 km WACCM $CO_2$ is smaller than MIPAS by 10–30% at most latitudes except near the polar summer where WACCM $CO_2$ is larger by about 20–40%. As was already found by *Garcia et al.* [2014], MIPAS $CO_2$ also favors a value of $Pr = 2$ (a larger eddy diffusion coefficient, $k_{zz}$), principally below around 100 km.

At altitudes above 95–100 km, in equinox, WACCM generally overestimates MIPAS $CO_2$ by about 40–80%, although it is limited to ±20% in the SH in September and October. For solstice conditions such overestimation is significantly smaller, with WACCM overestimating MIPAS $CO_2$ by only 5–20% at 50°–20° in the winter hemisphere and underestimating the $CO_2$ vmr at 30°–90° in the polar summer hemisphere. This almost general WACCM overestimation above 100 km might be explained by an underestimation of $CO_2$ photolysis, which is very coarse in WACCM at short wavelengths. However, this would lead to even larger WACCM $CO_2$ in the polar summer, which is not the case. A global reduction of the eddy diffusion coefficient by a factor of 2 would also reduce the $CO_2$ concentration at all latitudes and altitudes. Then, it is not clear which of the two processes could explain the differences or, if both, to what extent.

The WACCM and MIPAS $CO_2$ zonal mean fields, despite the very similar global features, also show some distinct patters that are likely attributed to dynamical processes. In particular, near 90–110 km in the polar summer region, the $CO_2$ isolines are closer and lower in MIPAS than in WACCM and suggest that the meridional circulation seems to be stronger in MIPAS than in WACCM. Thus, further studies of WACCM aspects like its photolysis parameterization at short wavelengths, its energy budget (in order to reproduce the measured temperatures) and the dynamical processes would be very useful.

We have shown deseasonalized monthly mean time series of ACE, SABER, MIPAS, and WACCM for the near global latitude coverage of 60°S–60°N at altitudes from 90 to 130 km. They show the good agreement between MIPAS and SABER at practically all altitudes in the 90–120 km range. ACE is in good agreement with MIPAS and ACE up to about 105 km, but it gradually becomes larger with altitude. WACCM underestimates the three instruments below about 100 km but gradually increases with altitude becoming in good agreement with all instruments at 100–110 km and halfway between MIPAS-SABER and ACE at 120 km. The three instruments and the model show a clear increase of the $CO_2$ vmr with time, more markedly at 90–100 km, where it is less affected by the solar cycle. Above about 110 km, ACE, MIPAS, and WACCM show a marked solar cycle signature, while it is less distinguishable in SABER data. A more detailed trend analysis of MIPAS $CO_2$ data is planned for the future.

# References

Beagley, S. R., C. D. Boone, V. I. Fomichev, J. J. Jin, K. Semeniuk, J. C. McConnell, and P. F. Bernath (2010), First multi-year occultation observations of $CO_2$ in the MLT by ACE satellite: Observations and analysis using the extended CMAM, *Atmos. Chem. Phys.*, *10*(3), 1133–1153.

Bermejo-Pantaleón, D., et al. (2011), Global observations of thermospheric temperature and nitric oxide from MIPAS spectra at 5.3 µm, *J. Geophys. Res.*, *116*, A10313, doi:10.1029/2011JA016752.

Bernath, P. F., et al. (2005), Atmospheric Chemistry Experiment (ACE): Mission overview, *Geophys. Res. Lett.*, *32*, L15S01, doi:10.1029/2005GL022386.

Boone, C. D., R. Nassar, K. A. Walker, Y. Rochon, S. D. McLeod, C. P. Rinsland, and P. F. Bernath (2005), Retrievals for the Atmospheric Chemistry Experiment Fourier–transform spectrometer, *Appl. Opt.*, *44*(33), 7218–7231.

Boone, C. D., K. A. Walker, and P. F. Bernath (2013), Version 3 retrievals for the Atmospheric Chemistry Experiment Fourier transform spectrometer (ACE-FTS), in *The Atmospheric Chemistry Experiment ACE at 10: A Solar Occultation Anthology*, edited by P. F. Bernath, pp. 103–127, A. Deepak Pub., Hampton, Va.

Edwards, D. P., M. López-Puertas, and R. R. Gamache (1998), The non-LTE correction to the vibrational component of the internal partition sum for atmospheric calculations, *J. Quant. Spectrosc. Radiat. Transfer*, *59*, 423–436.

Emmert, J. T., M. H. Stevens, P. F. Bernath, D. P. Drob, and C. D. Boone (2012), Observations of increasing carbon dioxide concentration in Earth's thermosphere, *Nat. Geosci.*, *5*(12), 868–871.

Eyring, V., et al. (2013), Overview of IGAC/SPARC Chemistry-Climate Model Initiative (CCMI) community simulations in support of upcoming ozone and climate assessments, *SPARC Newsletter*, *40*, 48–66.

Fischer, H., et al. (2008), MIPAS: An instrument for atmospheric and climate research, *Atmos. Chem. Phys.*, *8*, 2151–2188.

Funke, B., M. López-Puertas, G. P. Stiller, T. von Clarmann, and M. Höpfner (2001), A new non–LTE retrieval method for atmospheric parameters from MIPAS–Envisat emission spectra, *Adv. Space Res.*, *27*(6–7), 1099–1104.

Funke, B., M. López-Puertas, M. García-Comas, M. Kaufmann, M. Höpfner, and G. P. Stiller (2012), GRANADA: A generic radiative transfer and non-LTE population algorithm, *J. Quant. Spectrosc. Radiat. Transfer*, *113*(14), 1771–1817, doi:10.1016/j.jqsrt.2012.05.001.

Garcia, R. R., D. R. Marsh, D. E. Kinnison, B. A. Boville, and F. Sassi (2007), Simulation of secular trends in the middle atmosphere, *J. Geophys. Res.*, *112*, D09301, doi:10.1029/2006JD007485.

Garcia, R. R., M. López-Puertas, B. Funke, D. R. Marsh, D. E. Kinnison, A. K. Smith, and F. González-Galindo (2014), On the distribution of $CO_2$ and CO in the mesosphere and lower thermosphere, *J. Geophys. Res. Atmos.*, *119*, 5700–5718, doi:10.1002/2013JD021208.

García-Comas, M., et al. (2012), On the quality of MIPAS kinetic temperature in the middle atmosphere, *Atmos. Chem. Phys.*, *12*(12), 6009–6039.

Garcia, R. R., M. López-Puertas, B. Funke, D. E. Kinnison, D. R. Marsh, and L. Qian (2016), On the secular trend of $CO_x$ and $CO_2$ in the lower thermosphere, *J. Geophys. Res. Atmos.*, *121*, 3634–3644, doi:10.1002/2015JD024553.

García-Comas, M., et al. (2014), MIPAS temperature from the stratosphere to the lower thermosphere: Comparison of vM21 with ACE-FTS, MLS, OSIRIS, SABER, SOFIE and lidar measurements, *Atmos. Meas. Tech.*, *7*(11), 3633–3651.

Gil-López, S., et al. (2005), Retrieval of stratospheric and mesospheric $O_3$ from high resolution MIPAS spectra at 15 and 10 µm, *Adv. Space Res.*, *36*(5), 943–951.

Jurado-Navarro, A. A., M. López-Puertas, B. Funke, M. Garcia-Comas, A. Gardini, F. González-Galindo, G. P. Stiller, T. V. Clarmann, U. Grabowski, and A. Linden (2016), Global distributions of $CO_2$ volume mixing ratio in the middle and upper atmosphere from daytime MIPAS high-resolution spectra, *Atmos. Meas. Tech.*, *9*(12), 6081–6100.

Jurado-Navarro, A. A., M. López-Puertas, B. Funke, M. García-Comas, A. Gardini, G. P. Stiller, and T. von Clarmann (2015), Vibration-vibration and vibration-thermal energy transfers of $CO_2$ with $N_2$ from MIPAS high resolution limb spectra, *J. Geophys. Res. Atmos.*, *120*, 8002–8022, doi:10.1002/2015JD023429.

Kaufmann, M., O. A. Gusev, K. U. Grossmann, R. G. Roble, M. E. Hagan, C. Hartsough, and A. A. Kutepov (2002), The vertical and horizontal distribution of $CO_2$ densities in the upper mesosphere and lower thermosphere as measured by CRISTA, *J. Geophys. Res.*, *107*, 8182, doi:10.1029/2001JD000704.

Kunz, A., L. L. Pan, P. Konopka, D. E. Kinnison, and S. Tilmes (2011), Chemical and dynamical discontinuity at the extratropical tropopause based on START08 and WACCM analyses, *J. Geophys. Res.*, *116*, D24302, doi:10.1029/2011JD016686.

Laštovička, J., S. C. Solomon, and L. Qian (2011), Trends in the neutral and ionized upper atmosphere, *Space Sci. Rev.*, *168*, 113–145.

Lewis, H. G., A. Saunders, G. Swinerd, and R. J. Newland (2011), Effect of thermospheric contraction on remediation of the near-Earth space debris environment, *J. Geophys. Res.*, *116*, A00H08, doi:10.1029/2011JA016482.

Liou, J. C., and N. L. Johnson (2008), Instability of the present LEO satellite populations, *Adv. Space Res.*, *41*(7), 1046–1053.

Liu, H.-L., F. Sassi, and R. R. Garcia (2009), Error growth in a whole atmosphere climate model, *J. Atmos. Sci.*, *66*(1), 173–186.

López-Puertas, M., M. Á. López-Valverde, R. R. García, and R. G. Roble (2000), A review of $CO_2$ and CO abundances in the middle atmosphere, in *Atmospheric Science Across the Stratopause, Geophys. Monogr. Ser.*, vol. 123, edited by D. E. Siskind, S. D. Eckermann, and M. E. Summers, pp. 83–100, AGU, Washington, D. C.

López-Puertas, M., M. A. López-Valverde, C. P. Rinsland, and M. R. Gunson (1992), Analysis of the upper atmosphere $CO_2$ ($v_2$) vibrational temperatures retrieved from ATMOS/Spacelab 3 observations, *J. Geophys. Res.*, *97*, 20,469–20,478.

López-Puertas, M., and F. W. Taylor (1989), Carbon dioxide 4.3 µm emission in the Earth's atmosphere: A comparison between Nimbus 7 SAMS measurements and non-local thermodynamic equilibrium radiative transfer calculations, *J. Geophys. Res.*, *94*, 13,045–13,068.

López-Puertas, M., and F. W. Taylor (2001), *Non-LTE Radiative Transfer in the Atmosphere*, World Scientific Publ., Singapore.

López-Puertas, M., G. Zaragoza, M. Á. López-Valverde, and F. W. Taylor (1998), Non local thermodynamic equilibrium (LTE) atmospheric limb emission at 4.6 µm 2. An analysis of the daytime wideband radiances as measured by UARS improved stratospheric and mesospheric sounder, *J. Geophys. Res.*, *103*(D7), 8515–8530.

Offermann, D., and K. U. Grossmann (1973), Thermospheric density and composition as determined by a mass spectrometer with cryo ion source, *J. Geophys. Res.*, *78*(34), 8296–8304.

Rezac, L., A. Kutepov, J. M. Russell III, A. G. Feofilov, J. Yue, and R. A. Goldberg (2015a), Simultaneous retrieval of T(p) and $CO_2$ VMR from two-channel non-LTE limb radiances and application to daytime SABER/TIMED measurements, *J. Atmos. Sol. Terr. Phys.*, *130–131*, 23–42, doi:10.1016/j.jastp.2015.05.004.

Rezac, L., Y. Jian, J. Yue, J. M. Russell, A. Kutepov, R. Garcia, K. A. Walker, and P. Bernath (2015b), Validation of the global distribution of $CO_2$ volume mixing ratio in the mesosphere and lower thermosphere from SABER, *J. Geophys. Res. Atmos.*, *120*, 12067–12081, doi:10.1002/2015JD023955.

Rienecker, M., et al. (2011), MERRA: NASAś Modern-Era Retrospective Analysis for Research and Applications, *J. Clim.*, *24*, 3624–3648.

Rinsland, C. P., M. R. Gunson, R. Zander, and M. López-Puertas (1992), Middle and upper atmosphere pressure-temperature profiles and the abundances of $CO_2$ and CO in the upper atmosphere from ATMOS/Spacelab 3 observations, *J. Geophys. Res.*, *97*(D18), 20,479–20,495.

Roble, R. G., and R. E. Dickinson (1989), How will changes in carbon dioxide and methane modify the mean structure of the mesosphere and thermosphere?, *Geophys. Res. Lett.*, *16*, 1441–1444.

Sheese, P. E., C. D. Boone, and K. A. Walker (2015), Detecting physically unrealistic out liers in ACE-FTS atmospheric measurements, *Atmos. Meas. Tech.*, *8*(2), 741–750.

Smith, A. K., R. R. Garcia, D. R. Marsh, and J. H. Richter (2011), WACCM simulations of the mean circulation and trace species transport in the winter mesosphere, *J. Geophys. Res.*, *116*, D20115, doi:10.1029/2011JD016083.

Smith, A. K., et al. (2013), Satellite observations of ozone in the upper mesosphere, *J. Geophys. Res. Atmos.*, *118*, 5803–5821, doi:10.1002/jgrd.50445.

Trinks, H., and K. H. Fricke (1978), Carbon dioxide concentrations in the lower thermosphere, *J. Geophys. Res.*, *83*, 3883–3886.

Trinks, H., D. Offermann, U. von Zahn, and C. Steinhauer (1978), Neutral composition measurements between 90 and 220 km altitude by rocket-borne mass spectrometer, *J. Geophys. Res.*, *83*(A5), 2169–2176.

von Clarmann, T., et al. (2003), Retrieval of temperature and tangent altitude pointing from limb emission spectra recorded from space by the Michelson Interferometer for Passive Atmospheric Sounding (MIPAS), *J. Geophys. Res.*, *108*, 4736, doi:10.1029/2003JD003602.

Yue, J., J. M. Russell III, Y. Jian, L. Rezac, R. R. Garcia, M. López-Puertas, and M. G. Mlynczak (2015), Increasing carbon dioxide concentration in the upper atmosphere observed by SABER, *Geophys. Res. Lett.*, *42*, 7194–7199, doi:10.1002/2015GL064696.

Zaragoza, G., M. López-Puertas, M. Á. López-Valverde, and F. W. Taylor (2000), Global distribution of $CO_2$ in the upper mesosphere as derived from UARS/ISAMS measurements, *J. Geophys. Res.*, *105*, 19,829–19,839.